University of Alberta

Examination and Removal of Backgrounds for TWIST at TRIUMF

by

Robert Paul MacDonald

A thesis submitted to the Faculty of Graduate Studies and Research in partial fulfillment of the requirements for the degree of **Master of Science**.

Department of Physics

Edmonton, Alberta
Spring 2002

National Library of Canada
Acquisitions and Bibliographic Services
395 Wellington Street
Ottawa ON K1A 0N4
Canada

Bibliothèque nationale du Canada
Acquisitions et services bibliographiques
395, rue Wellington
Ottawa ON K1A 0N4
Canada

Your file Votre référence

Our file Notre référence

The author has granted a non-exclusive licence allowing the National Library of Canada to reproduce, loan, distribute or sell copies of this thesis in microform, paper or electronic formats.

The author retains ownership of the copyright in this thesis. Neither the thesis nor substantial extracts from it may be printed or otherwise reproduced without the author's permission.

L'auteur a accordé une licence non exclusive permettant à la Bibliothèque nationale du Canada de reproduire, prêter, distribuer ou vendre des copies de cette thèse sous la forme de microfiche/film, de reproduction sur papier ou sur format électronique.

L'auteur conserve la propriété du droit d'auteur qui protège cette thèse. Ni la thèse ni des extraits substantiels de celle-ci ne doivent être imprimés ou autrement reproduits sans son autorisation.

0-612-69734-7

Canada

University of Alberta

Library Release Form

Name of Author: Robert Paul MacDonald

Title of Thesis: Examination and Removal of Backgrounds for TWIST at TRIUMF

Degree: Master of Science

Year this Degree Granted: 2001

Permission is hereby granted to the University of Alberta Library to reproduce single copies of this thesis and to lend or sell such copies for private, scholarly or scientific research purposes only.

The author reserves all other publication and other rights in association with the copyright in the thesis, and except as herein before provided, neither the thesis nor any substantial portion thereof may be printed or otherwise reproduced in any material form whatever without the author's prior written permission.

Robert MacDonald.

Robert Paul MacDonald
10883 Saskatchewan Drive
Edmonton, AB
Canada T6E 4S6

Date: Oct. 24/01

"It has long been an axiom of mine that the little things are infinitely the most important."
—Sherlock Holmes in *A Case of Identity*, by A. Conan Doyle

University of Alberta

Faculty of Graduate Studies and Research

The undersigned certify that they have read, and recommend to the Faculty of Graduate Studies and Research for acceptance, a thesis entitled **Examination and Removal of Backgrounds for TWIST at TRIUMF** submitted by Robert Paul MacDonald in partial fulfillment of the requirements for the degree of **Master of Science**.

Dr. Nathan L. Rodning (Supervisor)

Dr. Marc deMontigny (External)

Dr. Andrzej Czarnecki

Dr. Glen Marshall

Dr. W. John McDonald

Date: 4 Oct 2001

Abstract

The *TWIST* experiment at TRIUMF will measure the muon decay spectrum to a greater precision than has ever been achieved. *TWIST* requires a highly polarized muon source; "surface" muons, from pion decay on the surface of the production target at the TRIUMF M13 beamline, provide such a source. "Cloud" muons, from pion decay in flight, as well as pions themselves, are experimental backgrounds. This thesis presents the results of a study of these backgrounds and ways to eliminate them. As shown in this study, cloud muons were found to have a polarization of 0.30 ± 0.02, in the direction opposite the surface muon polarization. At a beam momentum of 29.2 MeV/c, the beam composition was found to be: $(97.1 \pm 0.2)\%$ surface muons; $(2.4 \pm 0.2)\%$ cloud muons; and $(0.4 \pm 0.1)\%$ pions. This study also shows that these particles can be eliminated to better than a part in 10^4 while keeping more than 50% of the muons of interest, using a cut on particle time of flight.

Acknowledgements

I would like to thank Professor Nathan L. Rodning of the University of Alberta for his support, advice, and excellent supervision since September of 1999. The contributions of the *TWIST* collaboration and the TRIUMF μSR group are greatly appreciated. In particular, many thanks to Dr. Peter Green, Dr. Pierre-André Amaudruz, and especially Dr. Glen Marshall for their invaluable support and assistance.

My thanks, too, to my supervisory committee: Dr. Rodning, Dr. Marshall, Dr. Andrzej Czarnecki, Dr. W. John McDonald, and Dr. Marc deMontigny.

The funding from the National Science and Engineering Research Council, and the support of the University of Alberta, are gratefully acknowledged.

Finally, I am sincerely grateful to my friends, colleagues and family for their advice and support.

Contents

1 Introduction 1
- 1.1 Motivation and Objectives . . . 1
- 1.2 Overview of Experimental Method . . . 1
- 1.3 Summary of Chapters . . . 2

2 Theory of Muon Decay 3
- 2.1 Introduction and Motivation . . . 3
- 2.2 Kinematic Maximum Positron Energy . . . 3
- 2.3 General Form of Muon Decay . . . 3
- 2.4 The Michel Parameters . . . 4

3 Overview of the *TWIST* Experiment 7
- 3.1 The Goals of *TWIST* . . . 7
- 3.2 The *TWIST* Hardware . . . 8
- 3.3 Beam Requirements of *TWIST* . . . 9
- 3.4 Particle Identification with *TWIST* . . . 10

4 Production and Transport of Muons for *TWIST* 11
- 4.1 Beamline Overview . . . 11
  - 4.1.1 Measuring Cyclotron Timing and Current . . . 11
- 4.2 The M13 Beamline . . . 12
  - 4.2.1 Particle Phase Space . . . 13
- 4.3 Muon Production at the 1AT1 Target . . . 13
  - 4.3.1 1AT1 Target Materials . . . 13
  - 4.3.2 Pion Production and Decay . . . 14
  - 4.3.3 Surface Muons vs. Cloud Muons . . . 15
- 4.4 Calibrating Channel Momentum . . . 15

5 Introduction to μSR 21
- 5.1 Overview . . . 21
- 5.2 The μSR Spectrum . . . 22
  - 5.2.1 Angular Distribution of Decay Positrons . . . 22
  - 5.2.2 μSR Decay Time Spectrum . . . 23
- 5.3 Sample μSR Spectra . . . 24

6 The μSR Beam Study 26
- 6.1 Overview . . . 26
- 6.2 Apparatus . . . 26
  - 6.2.1 Particle Range Estimates . . . 29
  - 6.2.2 Data Acquisition System . . . 29
- 6.3 Data Taking . . . 30
  - 6.3.1 Production Target . . . 30
  - 6.3.2 TDC Calibration . . . 30

7 Beam Study Analysis and Results **35**
7.1 Analysis software 35
7.2 Time-of-Flight Structure of the Beam 35
7.2.1 Calculating Time of Flight 35
7.2.2 Time of Flight and Cyclotron Period 35
7.2.3 Time-of-Flight Structure at Surface Muon Momenta 36
7.2.4 Time-of-Flight Structure at Cloud Muon Momenta 39
7.3 Particle Identification 40
7.3.1 Time of Flight 40
7.3.2 Beam Scintillator ADC 41
7.4 Polarization Measurements 42
7.4.1 Beam Polarization at Cloud Muon Momenta 44
7.4.2 Beam Polarization at Surface Muon Momenta 46
7.5 μSR Simulation with GEANT 51
7.6 Selecting Surface Muons by CP Time-of-Flight 54
7.7 Particle Rates 55
7.7.1 Calibrating T1ION Scaler to Proton Beam Current 55
7.7.2 Rates at Surface Muon Momenta 56
7.7.3 Rates at Cloud Muon Momenta 59
7.8 Producing a Low-Polarization Muon Beam 59

8 Conclusion **63**

Bibliography **64**

A μSR Electronics **65**

Index **69**

List of Tables

3.1 The Michel Parameters: Standard Model predicted values, current values, and precision expected from *TWIST*. 7
3.2 Weak coupling constants: Standard Model predicted values, current experimental limits, and model-dependent limits expected from *TWIST*. 8

4.1 Summary of momentum scan results, both targets. 19

6.1 Summary of apparatus specifications. 28
6.2 Statistics on inter-peak spacings for Time Calibrator Histograms (figure 6.2). 30

7.1 Summary of relative polarizations for various beam particles. 44
7.2 Background levels for various CP Time-of-Flight cuts. 55
7.3 Surface muon, cloud muon, and pion rates vs. CP TOF bin, at 29.2 MeV/c (D scintillator); calculated using total beam asymmetry. 58
7.4 Surface muon and cloud muon rates at 26.3 MeV/c (D scintillator); calculated using total beam asymmetry. 58
7.5 Particle rates relative to total beam rate, 26.3 and 29.2 MeV/c. 58
7.6 Cloud muon and pion rates at 32.1 and 35.0 MeV/c (C scintillator); calculated using direct counts in CP TOF spectrum. 59
7.7 Total particle rates relative to total beam rate, 32.1 and 35.0 MeV/c. 59
7.8 Estimates of the momentum where the beam polarization is zero, for two CP cuts. 62

List of Figures

2.1 Michel Spectrum of muon decay. 5

3.1 The *TWIST* spectrometer. Polarized muons enter from the upper left, and are stopped in the target at the centre of the spectrometer. The chambers track the positrons as the spiral outwards along the beam axis. 9

4.1 Schematic of the M13 beamline. 12
4.2 Normalized muon rate vs. B1 magnetic field; Beryllium and Carbon production target data. 17
4.3 Simplified schematic of apparatus for counting muons and positrons. 18
4.4 Normalized positron rate vs. B1 magnetic field; Beryllium and Carbon 1AT1 target data. 20

5.1 Basic μSR apparatus schematic. 22
5.2 Comparison of μSR decay spectra from surface muons and cloud muons, with μSR fit functions. 25

6.1 Schematic of μSR apparatus. 27
6.2 Histogram of measurements taken using a Time Calibrator, for LeCroy 4208 and 2228A TDC's. 31
6.3 "Residuals" (spacing - mean spacing) measured for 4208 and 2228A TDC's. . 32
6.4 Result of a random trigger on the LeCroy 4208 and 2228A TDC's. 33

7.1 Raw CP Time-of-Flight histogram for surface muons (29.2 MeV/c). 37
7.2 CP Time-of-Flight histogram for surface muons (29.2 MeV/c), with corrections to the CP axis. 38
7.3 CP Time-of-Flight histogram for surface muons (26.3 MeV/c, 10% below the momentum in figure 7.2), with corrections to the CP axis. 38
7.4 Estimated locations of pion and cloud muon peaks at 29.2 MeV/c. 39
7.5 CP Time-of-Flight histogram for cloud muons (32.1 MeV/c), with corrections to the CP axis. 40
7.6 CP TOF histograms for cloud muons, at 32.1 and 35.0 MeV/c. 41
7.7 Histogram of ADC data for beam (C) scintillator, 32.1 MeV/c. 42
7.8 2D histogram of C scintillator ADC signal vs. CP TOF, 32.1 MeV/c. 42
7.9 Histograms of Decay time vs. CP Time-of-Flight, D scintillator. 44
7.10 Cloud muon decay spectrum (32.1 MeV/c data), and μSR fit function. 45
7.11 Cloud muon decay spectrum (35.0 MeV/c data), and μSR fit function. 46
7.12 Muon decay spectra for 32.1 MeV/c pion data, with μSR fits. 47
7.13 μSR fit parameters vs. CP Time-of-Flight, 29.2 MeV/c. 48
7.14 Surface muon decay spectrum (29.2 MeV/c data), and μSR fit function. . . . 49
7.15 μSR fit parameters vs. CP Time-of-Flight, 26.3 MeV/c. 50
7.16 Effect of air on muon polarization. 52
7.17 μSR spectrum from simulated surface muon data; DOWN TDC data, centred target. 53

7.18 μSR spectrum from simulated surface muon data; DOWN TDC data, offset target. 53
7.19 μSR spectrum from simulated pion data; UP TDC data, centred target. . . . 54
7.20 Calibration curve: T1ION scaler to integrated BL1A proton beam current. . 56
7.21 C scintillator rate vs. momentum, across surface muon edge. (30 Oct. data) . 60
7.22 Estimated surface and cloud muon rates, and beam polarization, vs. momentum; 9 ns "virtual CP cut" (whole cloud muon distribution). 61
7.23 Estimated surface and cloud muon rates, and beam polarization, vs. momentum; 2 ns "virtual CP cut" (cloud muon peak only). 61

A.1 Scintillator arrangement for μSR beam study. 66
A.2 Electronics for generating scintillator coincidence signals. 67
A.3 Schematic for data acquisition electronics. 68

List of Symbols

Acronyms

BL1A	A primary proton beamline at TRIUMF; see chapter 4
CP TOF	"CP Time-of-Flight"; the time between the arrival of a particle and the next Capacitive Probe pulse. See section 7.2.2.
M13	Secondary beamline at TRIUMF; see chapter 4
ns	Nanoseconds
T1ION	Pulser whose rate is proportional to BL1A proton current; see chapter 4 and p.55
TRIUMF	TRI-University Meson Facility
TWIST	TRIUMF Weak Interaction Symmetry Test; see chapter 3

Symbols

α	Asymmetry parameter in muon decay spectrum
β	Particle speed with respect to c ($\beta = v/c$)
ϕ	Precession phase parameter in muon decay spectrum
E	Particle total energy (in lab frame)
f	Muon precession frequency (in Hz)
m	Particle rest mass
p	Particle momentum
P_μ	Muon beam polarization
v	Particle speed (in lab frame)
x	The positron's "reduced energy": $x = E/E_{max}$, where E is the energy of the decay positron/electron, and E_{max} is the maximum possible energy (the decay cutoff).

Chapter 1

Introduction

1.1 Motivation and Objectives

TWIST, the TRIUMF Weak Interaction Symmetry Test, will study the muon decay spectrum (specifically, the decay $\mu^+ \to e^+\nu_e\overline{\nu_\mu}$) to very high precision, in order to explore the weak interaction. The decay spectrum depends on the spin direction of the muon, so to study this dependence *TWIST* needs muons which are highly polarized.

Pions which decay at rest in the production target of the M13 beam at TRIUMF produce muons which are almost completely polarized. The polarization of muons from in-flight pion decays depends on the beamline geometry, and is not 100% in general; these muons, as well as the pions themselves, are experimental background.

The M13 beam was studied in an effort to learn the properties (including polarization and rate) of the backgrounds, and to determine a method to eliminate them from the data. The study is the topic of this thesis.

1.2 Overview of Experimental Method

Scintillators were used to detect particles in this experiment. Beam positrons were removed from the data using a combination of a cut on the energy deposited in the main beam scintillator, and a positron veto using a second scintillator downstream of the stopping target.

Particle polarization was measured using a technique called μSR, or "Muon Spin Rotation," which uses the asymmetric angular distribution of positrons from muon decay, as well as the precession of the muon spin vector in a magnetic field. The angular distribution of positrons is part of what *TWIST* will measure to high precision, but it is currently known well enough to determine muon polarization to the precision of this beam study.

1.3 Summary of Chapters

Chapter 2 describes what we know about the decay of the muon, and explains how studying this process can lead to insight into the weak interaction. Chapter 3 introduces the *TWIST* experiment, its goals, and its requirements, which motivates this study. Chapter 4 explains how muons are created for the M13 beamline at TRIUMF, as well as what background particles are in the beam and where they originate. Chapter 5 covers the μSR technique and how it is applied to polarization measurements, and chapter 6 details the experiment performed to study the beam backgrounds using μSR . Chapter 7 contains the analysis of the data from the study, including polarization and rates of the background particles, recommends a method of culling backgrounds from the data using a cut on particle time of flight, and suggests possible uses for the background particles. Chapter 8 summarizes and concludes the study.

Chapter 2

Theory of Muon Decay

2.1 Introduction and Motivation

Muon decay is a very good system in which to study the weak interaction, since it is a purely leptonic process; only the weak and electromagnetic forces participate.

The momentum distribution of the positrons from muon decay (that is, the spectrum of directions and energies) is clearly predicted by the Standard Model. However, the experimental verification for this prediction is rather loose; careful study of the decay spectrum can either strengthen the Standard Model or reveal "new physics."

2.2 Kinematic Maximum Positron Energy

The positive muon's dominant decay mode (with a branching ratio of about 100%) is $\mu^+ \to e^+\nu_e\overline{\nu_\mu}$. (The negative muon's decay mode is simply the charge conjugate of this.) The positron from this decay can have a range of energies, since muon decay is a three-body process. The maximum energy a positron can have occurs when both neutrinos are emitted in the direction opposite the positron direction. Using conservation of momentum and energy, it can be shown that the positron's energy in this case, E_{max}, is given by

$$E_{max} = \frac{m_e^2 + m_\mu^2}{2m_\mu} \approx \frac{m_\mu}{2}. \tag{2.1}$$

(The approximation is a good one, since $m_\mu^2/m_e^2 \approx 45000$.)

Other decay modes of the positive muon are the inner bremsstrahlung decay, $\mu^+ \to e^+\gamma\nu_e\overline{\nu_\mu}$, with a branching ratio of 0.014 ± 0.004, and $\mu^+ \to e^+e^+e^-\nu_e\overline{\nu_\mu}$, with a branching ratio of $(3.4 \pm 0.4) \times 10^{-5}$. Branching ratios are from the Particle Data Book [7].

2.3 General Form of Muon Decay

The most general description of muon decay is one which allows any type of weak coupling (scalar (S), vector (V), or tensor (T)) between any combination of left-handed or right-

handed fermions.[1] The decay distribution in energy and angle then takes the form

$$\frac{d^2\Gamma}{dxd(\cos\theta)} \propto \left| \sum_{\substack{i=L,R \\ j=L,R \\ \kappa=S,V,T}} g_{ij}^{\kappa} < \overline{\psi_{e_i}}|\Gamma^{\kappa}|\psi_{\nu_e} >< \overline{\psi_{\nu_\mu}}|\Gamma_{\kappa}|\psi_{\mu_j} > \right|^2 \tag{2.2}$$

where Γ is the decay probability, $x = E_e/E_{max}$ is the positron's reduced energy, θ is the angle between the positron's momentum vector and the muon's spin vector, and Γ^{κ} are the interaction matrices given by combinations of the Dirac γ matrices:

$$\Gamma^S = 1,\ \Gamma^V = \gamma^\mu,\ \Gamma^T = \frac{1}{\sqrt{2}}\sigma^{\mu\nu} = \frac{i}{2\sqrt{2}}(\gamma^\mu\gamma^\nu - \gamma^\nu\gamma^\mu). \tag{2.3}$$

The coupling constants g_{ij}^{κ} must be measured. The Standard Model states that $g_{LL}^{V} = 1$ and all the other coupling constants are zero; this is done by fiat, because no direct evidence has been seen for any other type of weak interaction, but there is no real evidence *excluding* any other type of interaction, either. (The exceptions are g_{LL}^{T} and g_{RR}^{T}, which are identically zero because there are not enough degrees of freedom in the weak interaction to allow them. There are only 16 unique products of Dirac γ matrices, and all 16 can be written as the product of four or fewer γ's. The g_{LL}^{T} and g_{RR}^{T} couplings require the product of six γ's ($\gamma^\mu\gamma^\nu\gamma^5 = \gamma^\mu\gamma^\nu\gamma^0\gamma^1\gamma^2\gamma^3$), which can be reduced to other couplings. Including these interactions would be redundant.)

See table 3.2 on page 8 for the current experimental limits on the values of the g_{ij}^{κ}.

2.4 The Michel Parameters

Equation 2.2 can be rewritten much more concisely using the parametrization of Michel [9] (this form follows that found in [7], with the addition of the factor of pc/E) for the decay of a muon ($\mu^{\pm}$) (ignoring terms of order x_0^2):

$$\begin{aligned}\frac{1}{x^2}\frac{d^2\Gamma}{dxd(\cos\theta)} \quad \propto \quad & 3(1-x) + \frac{2\rho}{3}(4x-3) + 3\eta x_0\frac{(1-x)}{x} \\ & \pm P_\mu\xi\frac{pc}{E}\left(1 - x + \frac{2\delta}{3}(4x-3)\right)\cos\theta\end{aligned} \tag{2.4}$$

where θ is the angle between the muon spin and the electron momentum, $x_0 = m_e/E_{max}$ is the minimum allowable value of x, $P_\mu = |\vec{P}_\mu|$ is the degree of muon polarization, $p = |\vec{p}|$ is the positron momemtum, E is the electron energy, and ρ, δ, ξ, and η are the **Michel Parameters**. The factor of p/E is a correction to the asymmetric part of the distribution, due to the mass of the electron.[2]

[1] A right-handed fermion is defined in this context as one whose wavefunction is an eigenfunction of the $1-\gamma^5$ operator.

[2] The weak decay results in polarized electrons; conservation of angular momentum then gives an asymmetric decay distribution, as with the pion decay. p/E is the maximum allowable electron polarization.

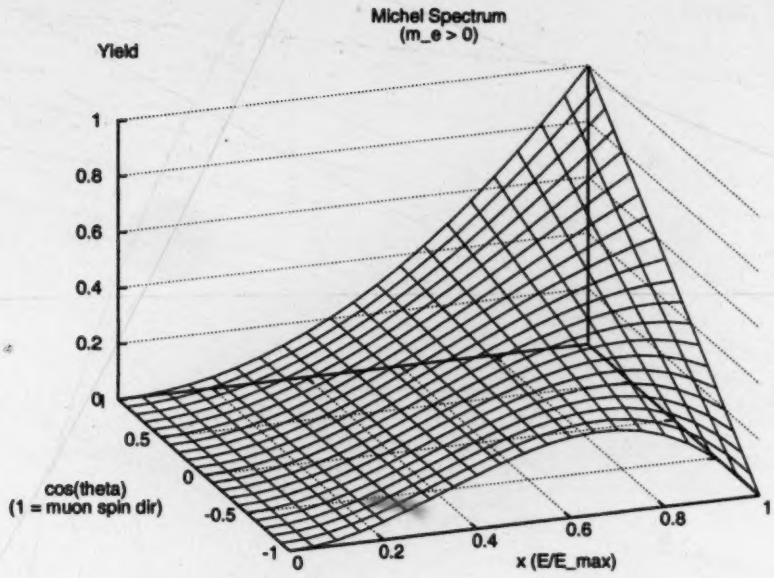

Figure 2.1: Michel Spectrum of muon decay (eqn. 2.4). Electron mass is included, but no radiative corrections.

This decay spectrum (with the x^2 factor moved to the right hand side) is plotted in figure 2.1.

The Michel parameters are given by:

$$\rho = \frac{3}{4} - \frac{3}{4}\Big[|g^V_{LR}|^2 + |g^V_{RL}|^2 + 2|g^T_{LR}|^2 + 2|g^T_{RL}|^2 + Re\left(g^S_{RL} g^{T\bullet}_{RL} + g^S_{LR} g^{T\bullet}_{LR}\right)\Big], \tag{2.5}$$

$$\xi\delta = \frac{3}{4} - \frac{3}{4}\Big[|g^V_{LR}|^2 + |g^V_{RL}|^2 + 4|g^T_{LR}|^2 + 2|g^T_{RL}|^2 + 2|g^V_{RR}|^2 + \frac{1}{2}|g^S_{RR}|^2 + \frac{1}{2}|g^S_{LR}|^2 + Re\left(g^S_{RL} g^{T\bullet}_{RL} - g^S_{LR} g^{T\bullet}_{LR}\right)\Big], \tag{2.6}$$

$$\xi = 1 - \Bigg[\frac{1}{2}|g^S_{RR}|^2 + \frac{1}{2}|g^S_{LR}|^2 + 2|g^V_{RR}|^2 + 4|g^V_{RL}|^2 - 2|g^V_{LR}|^2 - 2|g^T_{LR}|^2 + 8|g^T_{RL}|^2 + Re\left(g^S_{RL} g^{T\bullet}_{RL} - g^S_{LR} g^{T\bullet}_{LR}\right)\Bigg], \tag{2.7}$$

$$\eta = \frac{1}{2} Re\Big[g^V_{LL} g^{S\bullet}_{RR} + g^V_{RL}(g^{S\bullet}_{LR} + 6 g^{T\bullet}_{LR}) + g^V_{LR}(g^{S\bullet}_{RL} + 6 g^{T\bullet}_{RL}) + g^V_{RR} g^{S\bullet}_{LL}\Big]. \tag{2.8}$$

(taken from [10]). As mentioned, the Standard Model sets all weak coupling constants to zero except g_{LL}^{V}, so the Michel parameters have the values

$$\rho = \frac{3}{4}$$
$$\delta = \frac{3}{4}$$
$$\xi = 1$$
$$\eta = 0$$

Table 3.1 lists the current experimental limits on the Michel parameters.

Chapter 3

Overview of the *TWIST* Experiment

3.1 The Goals of *TWIST*

The Standard Model makes specific predictions about the muon decay spectrum, as described in chapter 2. Precise measurement of the spectrum, then, will either demonstrate the presence of "new physics" beyond the Standard Model, or constrain the effects that any new physics could have on the spectrum. The goal of the *TWIST* project—the Triumf Weak Interaction Symmetry Test—is to measure nearly the entire decay spectrum with high precision, something not yet done.

Table 3.1 compares the current experimental limits on the Michel parameters to the limits *TWIST* expects to achieve, as well as to the Standard Model values. A factor of approximately 10 improvement in the limits is expected on ρ, δ, and $P_\mu \xi$, and a factor of 3 improvement is expected on η. Table 3.2 compares the Standard Model predictions for the weak coupling constants g_{ij}^{γ} to the current experimental limits, and to the expected sensitivity of *TWIST*.

In the most general sense, each of the Michel parameters can be written in terms of the various weak coupling constants (section 2.4). There are many more than four coupling constants, so in order to constrain any of them assumptions must be made which depend

	Standard Model	Current Values	*TWIST* Precision
δ	3/4	$0.7486 \pm 0.0026 \pm 0.0028$	parts in 10^4
ρ	3/4	0.7518 ± 0.0026	parts in 10^4
$P_\mu \xi$	1	$1.0027 \pm 0.0079 \pm 0.0030$	parts in 10^4
η	0	-0.007 ± 0.013	parts in 10^3

Table 3.1: The Michel Parameters: Standard Model predicted values, current limits, and limits expected from *TWIST*. See equation 2.4 for definitions. Current values are from the Particle Data Book [7].

	Standard Model	Current Limits	TWIST (A)	TWIST (B)	TWIST (C)	TWIST (D)
$\lvert g^S_{RR}\rvert$	0	< 0.066	—	—	0.034	0.045
$\lvert g^V_{RR}\rvert$	0	< 0.033	0.012	0.017	0.017	0.022
$\lvert g^T_{RR}\rvert$	0	$\equiv 0$				
$\lvert g^S_{LR}\rvert$	0	< 0.125	—	—	0.034	0.046
$\lvert g^V_{LR}\rvert$	0	< 0.060	0.012	0.015	0.015	0.018
$\lvert g^T_{LR}\rvert$	0	< 0.036	—	0.010	—	0.013
$\lvert g^S_{RL}\rvert$	0	< 0.424	—	—	—	—
$\lvert g^V_{RL}\rvert$	0	< 0.110	0.012	0.012	0.012	—
$\lvert g^T_{RL}\rvert$	0	< 0.122	—	0.008	—	—
$\lvert g^S_{LL}\rvert$	0	< 0.550	—	—	—	—
$\lvert g^V_{LL}\rvert$	1	> 0.960	> 0.99977	> 0.99942	—	—
$\lvert g^T_{LL}\rvert$	0	$\equiv 0$				

Table 3.2: Weak coupling constants: Standard Model predicted values, current experimental limits (90% Confidence Level), and model-dependent limits expected from TWIST. Experimental limits are from the Particle Data Book [7]. Improved limits set by TWIST are based on the expected limits on the Michel parameters, and assume restrictions on which couplings are allowed: (A) V couplings only; (B) V and T couplings; (C) V and S couplings; (D) most general (V, S, and T) derivative-free couplings. TWIST improved limits taken from [10]. For the reasoning behind stating $|g^T_{RR}| = |g^T_{LL}| \equiv 0$, see section 2.3.

on the choice of weak interaction model. This choice is basically which types of couplings to allow, selected from: scalar (S), vector (V), and tensor (T); disallowing some coupling types reduces the number of free parameters in the muon decay distribution, allowing the limits on the Michel parameters to be converted into limits on the allowed weak coupling constants.

The Standard Model allows only vector couplings—specifically, constrained to couple to only left-handed fermions. In the notation of equations 2.4, only g^V_{LL} is non-zero in the Standard Model. There is no *a priori* reason for this, however, and in fact the limits on many of the other coupling constants are quite weak. TWIST will greatly improve the limits on many of the coupling constants, or find evidence of additional non-zero couplings.

3.2 The TWIST Hardware

The TWIST spectrometer is designed to measure the angles and energies of the positrons from muon decay. The muons stop in a target at the centre of a highly symmetric array of tracking chambers. The entire arrangement is in a ~ 2 Tesla magnetic field. The decay positrons follow helical paths, which are recorded by the tracking chambers; from the helices, the energies and angles of the positrons are reconstructed. See figure 3.1.

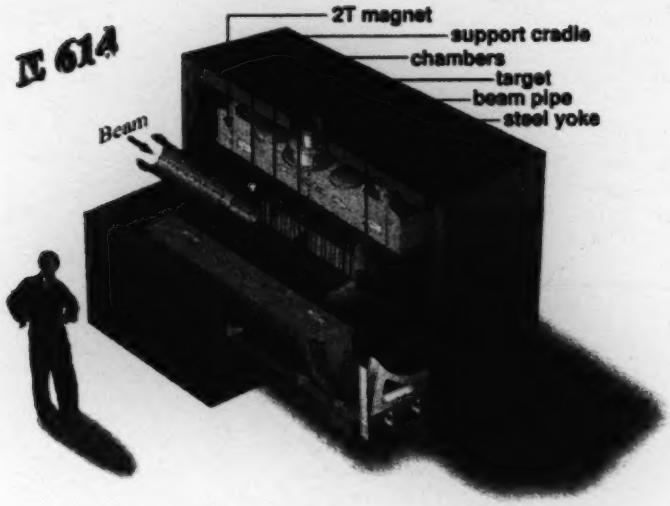

Figure 3.1: The *TWIST* spectrometer. Polarized muons enter from the upper left, and are stopped in the target at the centre of the spectrometer. The chambers track the positrons as the spiral outwards along the beam axis.

An important part of the *TWIST* experiment is that the incident muons are highly polarized. Pions decaying at rest naturally produce muons polarized along the muon momentum direction, because of the chirality of the neutrino and the conservation of angular momentum (see chapter 4 for details). *TWIST* will not directly measure the polarization, but will study sources of depolarization at the level of parts in 10000. There are background sources of muons with lower polarization; the beam study discussed in this thesis examined these background sources and what steps to be taken to reduce their effect on the data sample.

3.3 Beam Requirements of *TWIST*

As mentioned, *TWIST* requires a highly polarized muon beam for its measurements. This requires the identification and elimination of the backgrounds from the data with high efficiency.

There are also potential uses for the backgrounds, and the same identifying information will be important for this. Most useful will be an unpolarized or poorly polarized muon beam. There are two areas where low beam polarization would be useful: calibrating the spectrometer's energy measurements, and measuring the ρ Michel parameter.

As shown in figure 2.1, for a given angle close to the muon spin direction, the energy

distribution rises until it reaches the maximum (reduced energy $x = 1$), at which point it falls sharply to zero. This edge allows for a reliable energy calibration. However, for angles opposite the spin direction, the energy distribution decreases as it approaches the maximum energy, resulting in an unclear measurement of the cutoff energy.

Using an unpolarized beam has the effect of averaging over all angles with respect to spin direction. The result is a distribution which rises to the cutoff energy and falls sharply to zero for measurements in any direction. A beam of low polarization will achieve a similar effect: the distribution will be slightly higher or lower at different measured angles (relative to beam direction) but the cutoff energy will be nearly as sharp.

A poorly polarized beam will also be useful for measuring ρ. Consider the Michel spectrum again:

$$\frac{1}{x^2}\frac{d^2\Gamma}{dx d(\cos\theta)} \propto 3(1-x) + \frac{2\rho}{3}(4x-3) + 3\eta x_0 \frac{(1-x)}{x} \pm P_\mu \xi \left(1 - x + \frac{2\delta}{3}(4x-3)\right)\cos\theta$$

Here, θ is the angle between the muon spin and the emitted positron. By averaging the data over all θ, dependence on both δ and $P_\mu\xi$ is removed (since $\int_0^\pi \cos\theta = 0$), and the distribution basically depends entirely on ρ. The problem is that any asymmetries in the spectrometer efficiency will affect the average. Reducing P_μ shrinks the effect these asymmetries would have, and allows the determination of ρ from a data set with systematic uncertainties which differ from those when ρ is determined with polarized beam.

3.4 Particle Identification with *TWIST*

There are two main sources of background: pions, and low-polarization muons. Pions make up roughly 0.4% of the π/μ flux, and these background muons make up about 2% of the flux. By measuring the times of flight of particles through the *TWIST* beamline, these contributions can be virtually eliminated.

Roughly 20% of the incoming pions stop in the upstream "dense stack" [11], a region of the *TWIST* spectrometer with closely spaced tracking chambers. If their arrival time is noted and they are observed to decay into muons, they can be identified as pions. The identification efficiency needn't be very high to locate the pions in the time-of-flight distribution.

The polarization of the beam decreases by as much as 10% when the background muons are in the beam. This is well above the experimental limits on the Michel parameters (table 3.1). By counting the number of positrons which are emitted upstream vs. those emitted downstream, as a function of the arrival time of the decaying muons, this decrease in asymmetry can be observed and the flight time of the background muons can be determined.

Chapter 4

Production and Transport of Muons for *TWIST*

4.1 Beamline Overview

The cyclotron at TRIUMF produces several proton beams simultaneously. One of these beams—beamline 1A—is sent into the "Meson hall", where this beam study was done and where *TWIST* will be located. (Beamline 1B is also in the Meson hall; it used for proton irradiation of various materials and electronic chips.) The other two beams are sent to the "Proton hall" and the "ISAC hall".

Production targets are located at intervals along the 1A beamline; *TWIST* will use the first production target, labelled 1AT1. The particles produced or scattered from the production target are sent down secondary beamlines. Beamlines M11 and M13 take particles from 1AT1; M13 takes particles which leave the target at backward angles, and M11 takes forward-angle particles.

While M11 was designed for higher-momentum particles, the beam optics (magnets used to bend and focus the beam) in M13 were designed for low-momentum particles, and M13 is ideally suited for surface muons (at a momentum of ~ 30 MeV/c). *TWIST* plans to use M13 for this reason.

4.1.1 Measuring Cyclotron Timing and Current

The TRIUMF cyclotron produces protons in short (4 ns) bunches. In time with these bunches, a signal is sent to each experiment; this signal is called the "RF pulse" because it is synchronized to the RF used by the cyclotron to accelerate the protons. A capacitive probe on the 1A beamline directly detects the passage of proton bunches, and so provides an alternate source of cyclotron beam timing pulse. The latter was used for this beam study.

An ion chamber near the 1AT1 target produces electrical pulses whose rate is proportional to the 1A proton beam current. This signal is called "T1ION". The relationship

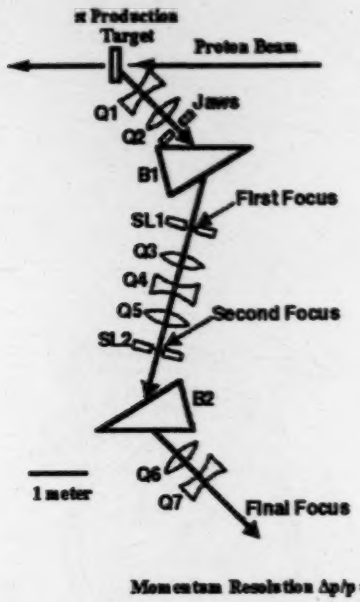

Figure 4.1: Schematic of the M13 beamline. Elements labelled "B" are dipole (bending) magnets; "Q" are quadrupole (focussing) magnets; "SL" are slits.

between the T1ION rate and the proton beam current is not entirely linear, however, and can drift over time. It was calibrated for this beam study, by comparing the measured T1ION pulse rate to the proton beam current listed by the TRIUMF control room.

4.2 The M13 Beamline

The M13 beamline consists of a series of dipole magnets, which bend the beam, and quadrupole magnets, which focus the beam. See figure 4.1 for a schematic.

The magnets are controlled by setting their currents. The fields in the dipole magnets (B1 and B2) are also monitored by NMR probes. No field monitoring is currently done for the quadrupole magnets, although the *TWIST* collaboration plans to change this in the future.

The fields in the various beamline magnets can be "tuned" to optimize beam characteristics (momentum selection, dispersion, emittance, focus position and shape, etc.). A *TWIST* technical note [4] by Jaap Doornbos discusses the tuning process in detail.

A quadrupole magnet can only focus the beam either horizontally or vertically; quads Q1, Q4, and Q7 are vertically-focusing, while quads Q2, Q3, Q5, and Q6 are horizontally-

focussing.

The dipole magnets are used for momentum selection. As the particles bend through the first dipole (B1) field, they are dispersed horizontally according to their momentum; they will therefore focus at different horizontal positions at the first beamline focus (F1). The F1HSL slit is used to select a narrow range of momenta. The F2HSL slit is used to clean up and improve the momentum selection. The second dipole (B2) reverses the effect of the first, combining the beam back into an undispersed ("achromatic") beam.

A set of vertical jaws and horizontal slits is located just upstream of B1, at a point called F0 (the "zeroeth" beam focus). These can be used to restrict the beam "emittance," or angular distribution, at a cost of restricting rate as well. These slits and jaws are labelled F0HSL and F0VJ.

The total path length from the 1AT1 production target to the centre of Q7 is 8.37 m. The distance from the centre of Q7 to the final focus can be controlled by changing the fields in Q6 and Q7.

The distance from the centre of Q7 to the upstream face of the *TWIST* yoke is about 1.3 m, for a total path length of $\sim$ 9.7 m from 1AT1.

The distance from the centre of Q7 to the centre of the detector used for this beam study (see section 6.2) is 1.26 m, for a total path length of 9.63 m from 1AT1.

4.2.1 Particle Phase Space

"Phase space" is the distribution of position and momentum for a given type of particle. It depends on the geometry of the particle source and of the beamline.

Surface muon beams have a relatively small phase space, because surface muons all come from a small source (the 1AT1 target). Cloud muon beams can have a much larger phase space, because these muons are produced over a larger area around the target, and so enter the beamline from a larger range of directions.

The slits and jaws at the start of the beamline (F0HSL and F0VJ) can be used to restrict the beam emittance and rate. However, since they block the edges of the beam, exactly how much they restrict a given particle type depends on the phase space for that component of the particle beam. This is an important consideration when comparing rate measurements from different runs; see section 7.7.1.

4.3 Muon Production at the 1AT1 Target

4.3.1 1AT1 Target Materials

There are basically two possibilities for 1AT1 target materials: carbon, and beryllium. The main difference is in the way they're cooled: the beryllium uses a water jacket, whereas the carbon is cooled by radiation and by conduction to its cooled support mounting.

A carbon target is preferred by *TWIST* for several reasons. Most important is the lack of a water jacket—the surface of the water jacket is the source of surface muons in the beryllium target. As Glen Marshall explains (private communication):

> Surface muon rate and luminosity depend critically on the distance of the region of pion production to the surface. The water jacket adds extra distance to its stainless steel surface which is the source of surface muons from the Be target. From direct measurements, the surface muon rate (and luminosity) is possibly 50% higher from the carbon target than from the Be target, depending on beam steering and other factors.
>
> The graphite target also gives us the possibility to customize the shape, without worrying so much about the water cooling requirements.

The greatest disadvantage to carbon is reliability. In the past, the size of a carbon target would slowly shrink, either through sublimation or through the flaking off of small pieces. In some cases, the brazing joint holding the target to the mount has been known to break, so that the target falls off the mount completely. None of these things are problems with the beryllium target. An effort to improve the reliability of the carbon target production has been initiated.

4.3.2 Pion Production and Decay

Nucleons in the target are held together by the strong force, which in a nuclear context is mediated by virtual pions. A proton passing through the target can interact with a virtual pion and make it real.

Pions are produced at a wide range of energies and at all angles. Those created with sufficiently low energy stop in the production target and decay there; the rest escape the target, and either enter the beamline wall or travel down one of the secondary beamlines.

All three types of pions (π^+, π^-, π^0) are created at the target. Since secondary beamlines are bent, they can carry only charged pions; the desired sign can be selected using magnet polarity. Because of the need for surface muons, *TWIST* will use only μ^+. Negative pions stopping in the target will be absorbed by the target nuclei.[13]

The pion decays almost exclusively into a muon and a muon neutrino; specifically:

$$\pi^+ \rightarrow \mu^+ + \nu_\mu$$

Using conservation of momentum, the muon and the neutrino must be emitted in opposite directions (in the pion rest frame). Assuming zero neutrino mass,

$$p_\mu = \frac{(m_\pi^2 - m_\mu^2)c}{2m_\pi} \tag{4.1}$$

which works out to 29.79 MeV/c.

Pions are spin 0 particles. By conservation of angular momentum, the spin of the muon must be opposite that of the neutrino, so that the sum is zero. The standard model does not allow for right-handed neutrinos, so the emitted muon has 100% polarization.

4.3.3 Surface Muons vs. Cloud Muons

We know that the muons which come from pions decaying at rest in the production target will be completely polarized[1], and that their polarization is opposite the direction of muon momentum (which is defined by the location and acceptance of the M13 beamline). Those which come from within the target, however, will scatter on their way out, lowering their polarization. The muons with the best polarization, then, are those which come from the surface of the production target—"surface" muons. Muons which come from deeper within the target will also lose energy on their way out, so selecting the momentum of the M13 beamline correctly will eliminate most of the scattered muons. The M13 beamline has a momentum acceptance of $\Delta p/p \sim 1\%$, which corresponds to a $\sim 20\mu$m thick layer of production target material. (That is, the muons at the low end of the 1% momentum range originated about 20 μm deeper in the target than those at the high end.) *TWIST* will use surface muons for their extremely high polarization.

Many pions escape the production target and decay in flight. In the rest frame of the laboratory, then, there are two ways to produce a muon with a given momentum: a pion travelling at a lower momentum which emits the muon in the forward direction; or a pion travelling at a higher momentum which emits the muon backward. The direction at which the muon is emitted determines that muon's spin direction, so these two processes result in muons of opposite polarization and the same momentum. Muons from in-flight pion decays are called "cloud" muons, and are considered by *TWIST* to be background contamination.

Cloud muons must be produced almost immediately after the pions themselves—otherwise, the pions will have left the area around the target, and the muons will not enter M13—and so they occur in narrow pulses every $\sim$ 43 ns cyclotron cycle. Surface muons come from stopped pions, so the pions can take their time decaying; their production therefore follows a pion decay curve with a lifetime of 26 ns, repeating every cyclotron cycle.

4.4 Calibrating Channel Momentum

Momentum selection is done by changing the B1 magnetic field (the other magnets in the beamline are changed proportionally to maintain the tune). Although the relationship between beam momentum and the B1 field setting can be calculated theoretically, it is

[1]This assumes a very well-defined channel acceptance: accepting muons travelling in a range of angles reduces the polarization. More fundamentally, it assumes that pion decay behaves according to Standard Model predictions sufficiently closely.

simpler and more reliable to simply measure it—the position of the production target, the B1 slit position, and fields of neighbouring magnets could all affect the calibration. This section is mostly a summary of a *TWIST* technote [8]. See that document for more details.

The "surface muon edge" is commonly used for this calibration at low energies. No surface muons can be produced with momenta higher than 29.79 MeV/c (as explained in section 4.3.2), so the surface muon rate drops to zero above this momentum. The cloud muon rate is roughly constant around this momentum (actually increasing very slowly with momentum), and experiences no such cutoff; the same holds for pions. Since the surface muon rate is much higher than that of cloud muons at this momentum, measuring the muon rate as a function of B1 magnetic field (and hence channel momentum) will show a strong drop, or edge, at exactly 29.79 MeV/c. (It will not be a vertical drop, because of the finite momentum acceptance—or "momentum bite"—of the beamline.)

Scans were performed using both carbon and beryllium 1AT1 targets (see section 4.3.1), using various F0 slit and jaw settings. Some of the later scans were performed using a different detector setup.

The scans were performed to measure two quantities: the B1 field strength at the surface muon edge; and the momentum bite, which represents the channel's momentum resolution. Channel momentum refers to the central momentum selected, so that roughly half the accepted momentum range is below the selected momentum, and half is above. When the channel momentum is set to 29.79 MeV/c, only half of the accepted momentum range can include surface muons; 29.79 MeV/c should therefore correspond to halfway down the edge in a momentum scan.

Momentum bite is defined as $\Delta p/p$, where Δp is the full width of the momentum distribution and p is the central momentum of the channel. The channel momentum is directly proportional to the B1 field strength B, so $\Delta p/p = \Delta B/B$. When plotting muon rate vs. B1 field, the width dB of the edge and the position of its centre are used to give the momentum bite.

Momentum bite is controlled by the width of the F1 Horizontal Slit (F1HSL). A very rough estimate by Dr. J. Doornbos is a momentum bite of 1% for every 1.25 cm of slit width; the F1HSL setting was 2.5 cm.

If the surface muon edge is approximated by a falloff with infinite slope, and the momentum bite is approximated by an inverted square well, then the convolution of the two will result in a falloff of flux from 100% to 0% over the range of the momentum bite. Figure 4.2 shows that this falloff takes place over about 2.2% of the dipole field, in rough agreement with Dr. Doornbos's estimate.

To count muons, an arrangement like the one sketched in figure 4.3 was used. (Two different physical apparatus were actually used, depending on when each scan was taken,

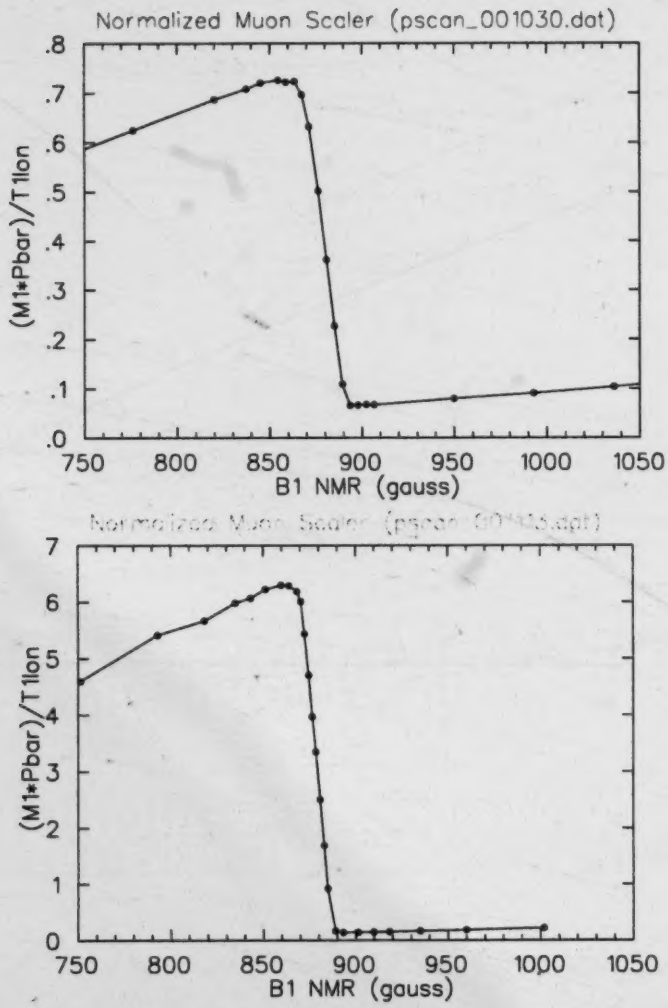

Figure 4.2: Normalized muon rate vs. B1 magnetic field. Top: 30 October data, Beryllium production target. Bottom: 13 November data, Carbon production target. Muon rate is normalized to T1ION rate (proportional to B1 proton current). Note the different vertical scales; see text.

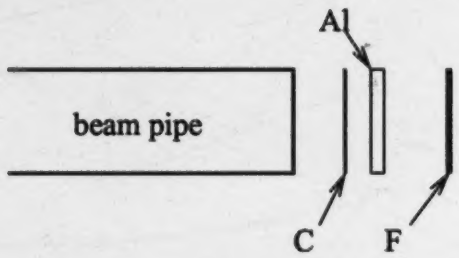

Figure 4.3: Simplified schematic of apparatus for counting muons and positrons. C is a very thin scintillator; F is much thicker. Al is an aluminum plate. (Not to scale.)

but for the purposes of these scans they operated the same way.) C is a very thin scintillator, sensitive to muons but not very sensitive to positrons; F is sensitive to both. A muon will make a signal in C and stop in the aluminum target, so $C \cdot \bar{F}$ makes a reliable muon trigger. (This trigger will count pions for the same reason. The pion rate is sufficiently constant over this region that they should not affect the results.) A positron will pass through the entire detector, leaving no signal above threshold in C but a signal in F, so F makes a reliable positron trigger.

The above triggers are counted simultaneously for a fixed amount of time (eg. 10 seconds). T1ION pulses are counted over the same time; this total is proportional to the number of protons which passed the 1AT1 target. Dividing a trigger count by the T1ION count gives a "normalized" particle count. It is important to note that the relationship between the T1ION rate and the M13 current (muon rate, positron rate, etc.) can vary, depending on slit and jaw settings, internal drift, and other factors, so it is difficult to compare normalized rates between scans. The relation should be constant within a scan, however, so the location of the edge can be meaningfully compared.

Using these triggers, the muon rate can be measured for various B1 field settings (this is what's meant by a "momentum scan"). Figure 4.2 shows two of these scans, one with a beryllium target at 1AT1, the other with a carbon target. The shapes are very similar—most of the differences are due to the slightly different point spacing—but the vertical scales are very different. One reason for this is that the scans used different slit and jaw settings: both scans used an F0 Horizontal Slit (F0HSL) setting of 80 mm, but the October 30 scan (beryllium target) had the F0 Vertical Jaws (F0VJ) set to 40 mm, while the November 13 scan (carbon target) had the F0VJ set to 25 mm. Another is that the beamline was being "tuned" between scans, which can result in different muon rates. Also, different target materials are known to produce different particle rates. The reason for the different scales was not pursued; the shape and the location of the edge are the important features.

Two more scans were done, one each for the beryllium and carbon targets, with similar

Beryllium target	**30 Oct.**	**5 Dec.**
B1 Field at Edge (Gauss)	879.6 ± 0.4	876.5 ± 0.4
Momentum bite	2.1%	1.3%
Graphite target	**13 Nov.**	**20 Nov.**
B1 Field at Edge (Gauss)	878.7 ± 0.4	877.8 ± 0.4
Momentum bite	1.6%	1.7%

Table 4.1: Summary of momentum scan results, both targets.

results. See [8].

Table 4.1 has a summary of the measured position and width ($\Delta B/B$) of the surface muon edge. Uncertainties quoted for magnetic fields represent the precision to which the B1 field can be controlled. No other uncertainties are included. No uncertainties were calculated for momentum bite. These measurements were sufficient for the purposes of this beam study, but should be repeated with greater care for *TWIST*.

Once the B1 field value at the surface muon edge has been found, the channel momentum is assumed to scale linearly with the B1 field.

Also of interest is the positron rate vs. B1 field. This is given in figure 4.4 for the same scans (one with beryllium at 1AT1, one with carbon) as those in figure 4.2. There are no "edges"—sudden drops or rises in the rate, similar to the surface muon edge—in the positron rate in this momentum region, so the curve should be smooth. As seen in the plots, there are some nonlinear features, especially near the surface muon edge (where the data points are densest). At first these were thought to be the result of some sort of hysteresis in the magnets—the magnet was not adjusted monotonically in the first scan—but most features were reproduced in later monotonic scans. The origin of these features is not clear. (The small spikes around 850 and 900 Gauss in the 30 October plot (top plot in figure 4.4) were not reproduced in later scans, using either carbon or beryllium targets.) The vertical scale changes from scan to scan, for the same reasons as it does for the muon rate plots.

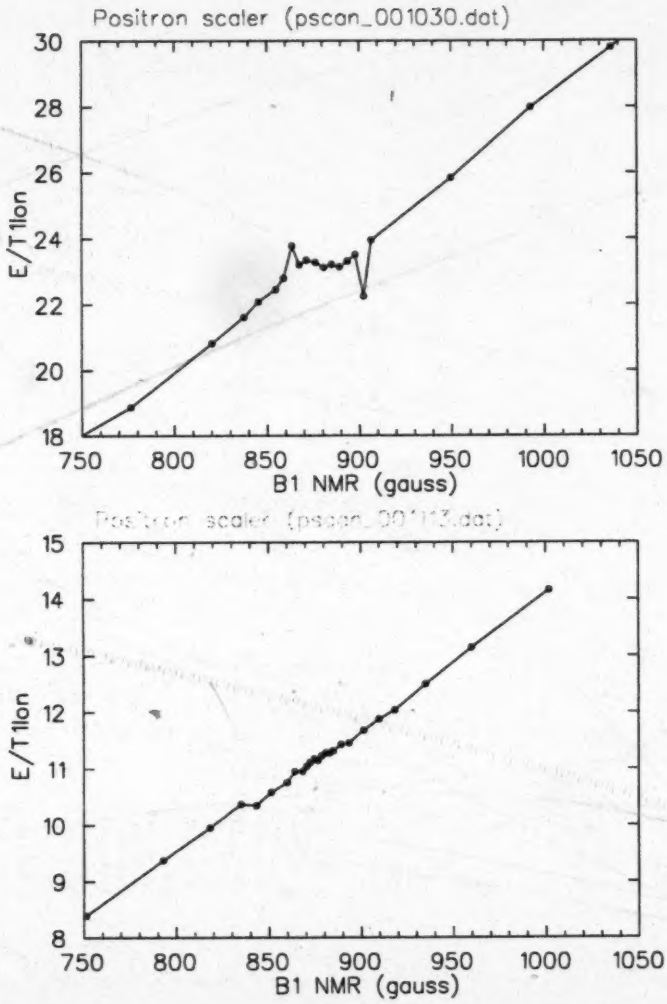

Figure 4.4: Normalized positron rate vs. B1 magnetic field. Top: 30 October data, Beryllium production target. Bottom: 13 November data, Carbon production target. Positron rate ("E") is normalized to T1ION rate (proportional to B1 proton current). The region with the densest data points (around 850–900 Gauss) corresponds to the surface muon edge. Note the different vertical scales; see text.

Chapter 5

Introduction to μSR

5.1 Overview

μSR stands for Muon Spin Rotation (or Relaxation, or Resonance). The technique uses the asymmetric decay distribution of the muon (section 2) and the fact that the muon spin precesses[1] in a magnetic field ("Larmor precession"). It is often used to examine the magnetic properties of materials, since the rate of precession is directly proportional to the field strength. (The name μSR was chosen to invoke the similarities to NMR experiments.) The TRIUMF μSR group web page[2] and the review article in the Encyclopedia of Applied Physics [2] have further information on many μSR applications.

μSR can be performed with negative muons, but positive muons are more often used. Negative muons have a strong chance of forming "muonic atoms"—replacing an electron in an atom. This process destroys the muon polarization. *TWIST* will use positive muons for its experiment, and so did this beam study.

Whereas in condensed matter physics, μSR is used to study magnetic properties of materials (by measuring the Larmor precession frequency of the muons), for this beam study the μSR technique was used differently: the magnetic field is assumed known (measured with a Gaussmeter), and the polarization of the incident muon beam is measured.

As shown in chapter 2, the angular distribution of positrons from decaying muons is not uniform; it depends on the angle between the decay positron and the muon spin direction. (The distribution is called the Michel spectrum.) More positrons are emitted in the direction of muon spin. (For negative muons, more electrons are emitted opposite the muon spin direction.)

Figure 5.1 shows a schematic of a simple μSR apparatus. A muon, polarized along the beam axis (parallel or antiparallel), enters the apparatus through a thin scintillator ("C"). The muon stops in the target. Until it decays, its spin precesses about the magnetic field supplied by the Helmholtz coils. When it decays, a positron is emitted in a random direction

[1] If the spin is not perpendicular to the magnetic field, only the perpendicular component will precess.
[2] `http://www.triumf.ca/msr/musr/musr_home.html`

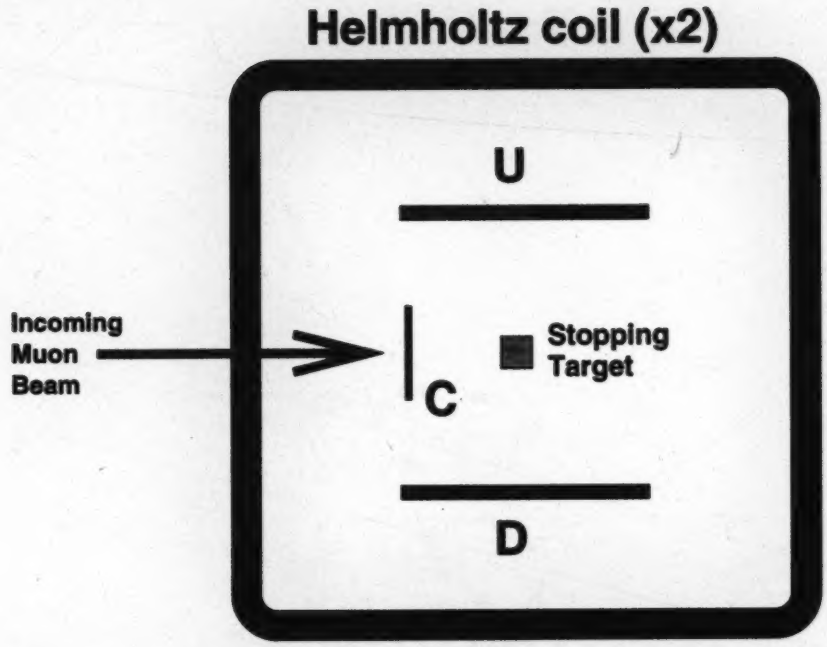

Figure 5.1: Basic μSR apparatus schematic. C is a thin ($\sim$ 0.1 mm) scintillator, for counting incoming muons. U and D are thick ($\sim$ 1 cm) scintillators, for counting decay positrons. The Helmholtz coils provide a uniform magnetic field throughout the stopping target, perpendicular to the muon beam axis. See text for more details.

(governed by the Michel Spectrum); if that positron should happen to pass through one of the thick scintillators ("U" or "D"), the decay time (the time between the C and U or D signals) is recorded.

Since the muon spin is precessing, and positrons are more likely to be emitted in the direction of spin, the decay spectrum for the muon beam has oscillations superimposed on the exponential decay curve. As shown in section 5.2, the frequency of these oscillations depends on the magnetic field, and the amplitude depends on the beam polarization.

5.2 The μSR Spectrum

5.2.1 Angular Distribution of Decay Positrons

Consider a beam of positive muons stopping in the target, with overall beam polarization $(0, 0, P_\mu)$ ($P_\mu \in [0, 1]$). (For negative muons, replace P_μ with $-P_\mu$ in these equations.) The distribution of angles and energies of the emitted positrons is given by the Michel spectrum,

described in chapter 2, as follows (neglecting electron mass and radiative corrections):

$$\frac{d^2\Gamma}{dxd(\cos\theta)} \propto x^2\left(3(1-x)+\frac{2}{3}\rho(4x-3)+P_\mu\xi\left[1-x+\frac{2}{3}\delta(4x-3)\right]\cos\theta\right) \tag{5.1}$$

where: $x = E_e/E_{max}$ is the "reduced energy" of the emitted positron, θ is the angle between the polarization axis and the emitted positron direction, Γ is the decay probability per unit time, and ρ, ξ, and δ are the "Michel parameters". See chapter 2 for details.

We can condense this equation down to

$$\frac{d^2\Gamma}{dxd(\cos\theta)} \propto F(x)[1+\alpha(x)\cos\theta] \tag{5.2}$$

where $\alpha(x)$, the anisotropic part of the spectrum, is known as the asymmetry. Assuming Standard Model values for the Michel parameters:

$$\alpha(x) = P_\mu\frac{2x-1}{3-2x} \tag{5.3}$$

and

$$F(x) = 2x^2(3-2x) \tag{5.4}$$

In a μSR experiment, the energy of the outgoing positron is not measured, so we integrate over x to find the energy-independent isotropic part of the distribution:

$$\int_{E_{min}}^{1} F(x)dx \approx 1 \tag{5.5}$$

and the energy-independent anisotropic part:

$$\int_{E_{min}}^{1} F(x)\alpha(x)dx \approx \frac{P_\mu}{3} \tag{5.6}$$

E_{min} is a low-energy cutoff due to energy losses in materials (such as the stopping target, and dead layers (eg. foils) of the counters); positrons with energy below E_{min} will not be detected. The approximations above hold as long as E_{min} is close to zero. The angular distribution of decay positrons is then given by

$$\frac{d\Gamma}{d(\cos\theta)} \propto 1+\frac{P_\mu}{3}\cos\theta. \tag{5.7}$$

5.2.2 μSR Decay Time Spectrum

The spectrum of muon decay times follows an exponential decay curve. However, if the muon's spin is precessing, a detector is more likely to see a decay positron if the spin vector is pointing towards it than when it is pointing away. This introduces oscillations to the spectrum.

The usual decay time spectrum is given by

$$N = N_0e^{-t/\tau} + B \tag{5.8}$$

where N is the number of decays at time t, τ is the muon lifetime, B is the constant background level (eg. from other beam particles), and N_0 is the overall normalization. The μSR decay time spectrum is given by

$$N = N_0 e^{-t/\tau}[1 + \alpha \cos(2\pi f t + \phi)] + B \tag{5.9}$$

where f is the Larmor precession frequency, ϕ is the initial phase of the oscillation, P_μ is the beam polarization (which is still along the z-axis, but we allow it to vary between 1 and -1), and α is called the **asymmetry**. Under "ideal" conditions, α is $P_\mu/3$ as given by equation 5.6; in reality, the value of α depends on the apparatus geometry, detector material and other characteristics, target materials, efficiency, energy thresholds, etc.[12]

It is important to note that, regardless of other factors determining the asymmetry, α is directly proportional to the beam polarization P_μ.

The initial phase ϕ depends on the selection of the zero time of the decay spectrum, detector geometry, etc. See section 7.4 for details.

The precession frequency f is given by the muon's gyromagnetic ratio γ_μ as follows:

$$f = \frac{\gamma_\mu}{2\pi} B = \frac{1}{2\pi} \frac{e}{m_\mu} B \tag{5.10}$$

where B is the magnetic field , e is the electric charge, and m_μ is the muon mass. Numerically, $\gamma_\mu/2\pi = 1.3553879(9) \times 10^8$ Hz/T.

5.3 Sample μSR Spectra

Figure 5.2 (a) shows the μSR decay spectrum for "surface" muons, which are almost fully polarized opposite the beam direction (ie. $P_\mu \approx -1$). Figure 5.2 (b) shows the μSR spectrum for "cloud" muons, which have a polarization of $P_\mu \approx 0.3$ along the beam direction. The oscillations are much less pronounced, and α has the opposite sign (equivalent to a change in phase by π—ie. a reversal in polarization direction). See section 7.4 for analysis. (As explained in that section, the χ^2/dof value should be ignored in these figures.)

(a) Surface muons:

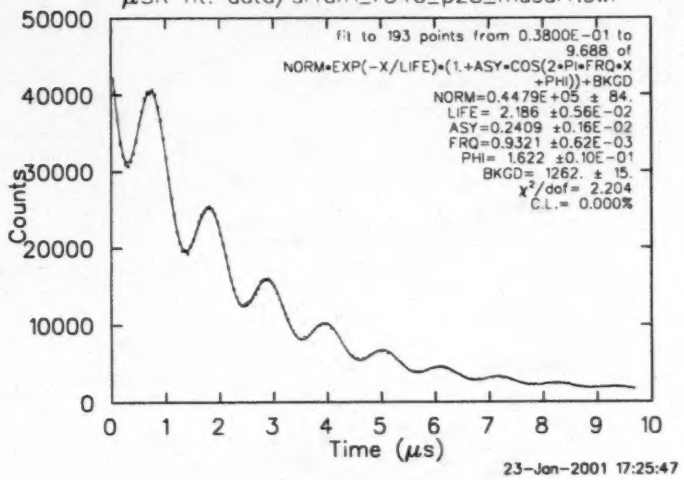

(b) Cloud muons:

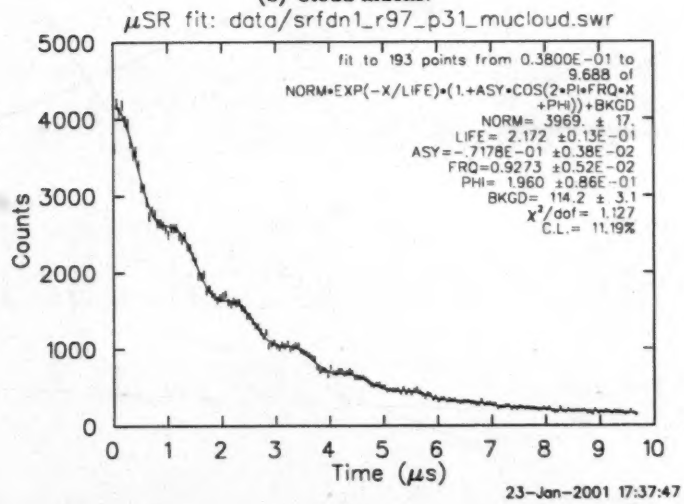

Figure 5.2: Comparison of μSR decay spectra from surface muons (fig. a) and cloud muons (fig. b), with μSR fit functions.

Chapter 6

The μSR Beam Study

6.1 Overview

The μSR technique described in chapter 5 was used to study the polarization of "background" particles at the end of the M13 beamline, particularly in relation to their arrival time relative to the 43 ns cyclotron period.

One of the main goals of this beam study was to measure the polarization of the cloud muons relative to that of the surface muons. The surface muons are assumed to be 100% polarized—this is true to within the precision of this experiment.

Another important goal of the study was to determine the time-of-flight (TOF) structure of the beam—the arrival times of particles, possibly different for each type. Once this is known, cuts on this arrival time can be used to remove most of the background particles.

Studying the overall polarization of the beam as a function of the TOF also allows for a more detailed assessment of the beam backgrounds.

The rates of the various particle types relative to the surface muon rate are an important consideration for any discussion of backgrounds; an additional goal of this study was to measure these rates.

6.2 Apparatus

For the μSR beam study, the LAMPF μSR spectrometer was used, supplied by the TRIUMF μSR group.[1] LAMPF includes three water-cooled Helmholtz coils and a wide variety of scintillators; this μSR beam study used only the innermost Helmholtz coil, and five flat scintillators, as shown in figure 6.1. The C scintillator is very thin (about 0.1 mm), and was used as a beam counter. The F, B, U, and D scintillator pairs are thick (about 1 cm), and were used to count decay positrons. The inner F counter (FI) was also used to veto beam positrons, which would pass through the target; the basic system trigger was $C \cdot \overline{FI}$. See appendix A for details of the electronics used.

[1] More information about the μSR group is available at: `http://musr.triumf.ca/`

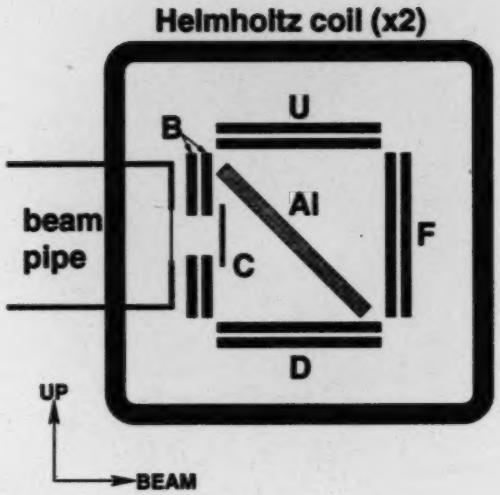

Figure 6.1: Schematic of LAMPF μSR apparatus. The Helmholtz coils were set to provide a magnetic field of approximately 70 Gauss at the target, aligned into (or out of) the page in this figure. Al is the aluminum stopping target. C, F, B, U, and D scintillators. See text for details.

Table 6.1 has a summary of the specifications of the apparatus.

The current in the Helmholtz coils was set to roughly 42 Ampères, to provide a magnetic field of about 70 Gauss (in the horizontal direction, perpendicular to the beam axis). This yields a muon precession period near 1 microsecond, or about half of the mean lifetime of the muon.

The precession of the muons is measured by taking the time between a signal in C (ie. the incoming muon) and a signal in a positron scintillator pair (indicating the passage of a decay positron through the pair). Requiring a signal in both the inner and outer scintillators of a pair served to reduce spurious TDC stops from scintillator noise. Each pair is treated as a single scintillator throughout this document, including in table 6.1. C is only a single scintillator; it was necessary to keep this scintillator as thin as possible, since the range of 30 MeV/c muons in scintillator is only about 1 mm.

The target used was a small aluminum plate, 0.75 ± 0.05 mm thick and much larger than the beam diameter. (For channel momenta above 29.2 MeV/c, two more plates of the same thickness were stacked on top of this one. This was done because the range of a 35 MeV/c muon in aluminum is about 1 mm.) The plate was leaned against the scintillators, so that it stood slightly less than 45° from vertical. It was "mounted" this way for two reasons: it was a very convenient method of support; and (more importantly) decay positrons have very little aluminum to travel through to reach the scintillators, compared to a vertical mounting. (If the plate was vertical, positrons traveling straight up or down would have to

Helmholtz coil:	
Separation (inner face to inner face):	22.0 ± 0.5 cm
Coil thickness:	3.5 ± 0.2 cm
Inner coil diameter:	23.5 ± 0.5 cm
Coil current:	~ 43 A
Magnetic field:	68.75 ± 0.05 Gauss
Scintillators:	
Distance from Q7 yoke face to B:	1.03 ± 0.02 m
C thickness:	0.125 ± 0.001 mm
Total B thickness:	1.4 ± 0.1 cm
Total F thickness:	1.4 ± 0.1 cm
Total U thickness:	1.3 ± 0.1 cm
Total D thickness:	1.3 ± 0.1 cm
Separation between B and F:	9.0 ± 0.5 cm
Separation between U and D:	8.5 ± 0.5 cm
Length of F (and B):	~ 8 in
Height of F (and B):	~ 7.5 in
Length of U (and D):	~ 8 in
Width of U (and D):	~ 3 in
Distance from 1AT1 to C:	~ 9.4 m
C offset w.r.t. beam centre:	~ 1 mm $\leftarrow$
(looking upstream)	~ 4 mm $\uparrow$
Aluminum Stopping Target:	
Thickness (< 30 MeV/c):	0.75 ± 0.05 mm
Thickness (> 30 MeV/c):	2.3 ± 0.2 mm
Orientation:	$\sim 40°$ from vertical
Effective thickness (along beam) (< 30 MeV/c):	~ 1 mm
Effective thickness (along beam) (> 30 MeV/c):	~ 3 mm

Table 6.1: Summary of apparatus specifications. The coil magnetic field was measured using the muon precession frequency from μSR measurements. The "Al Stopping Target" section describes the target used for 29.2 MeV/c channel momentum; at higher momentum two additional plates were added, each with the same dimensions.

pass through half the plate.)

The "effective" plate thickness (thickness along the beam axis) is about 1.0 mm. A 29.8 MeV/c muon stops at about 0.37 mm in aluminum.

The distance between the centre of the last quadrupole magnet (Q7) to the centre of the LAMPF apparatus was measured to be 1.261 ± 0.005 m. The distance from the 1AT1 production target to the centre of Q7 is 8.37 m. The total path length from the production target to the aluminum stopping target is then 9.63 m. The C scintillator was upstream of the LAMPF centre by 1.5–2 cm, placing it slightly more than 9.6 m from the production target.

6.2.1 Particle Range Estimates

To estimate the ranges of particles through material, the program DERANG, by Glen Marshall of TRIUMF, was used. Given the particle to simulate, and a list of materials (defined by chemical composition) through which the particle is to pass, DERANG returns the amount of energy lost in each "layer" of material, and at what average position the particles will stop.

Using this program, it was found that, at 29.7 MeV/c, muons in this apparatus will stop about 0.37 mm into the aluminum target. At cloud muon momenta, around 35 MeV/c, they pass through almost 1 mm of aluminum before stopping; for this reason, extra aluminum was added for studies at cloud muon momenta.

6.2.2 Data Acquisition System

This section is intended to provide an overview of the data acquisition (DAQ) electronics. See appendix A for details and circuit diagrams.

The **primary trigger** was $C \cdot \overline{FI}$—that is, an incoming beam particle which stops in the aluminum target. (Only the inner scintillator (FI) of the F pair was used in this trigger.) A pile-up gate (PUG) was used to protect against a second muon entering the apparatus before the first one decays (a 10 μs gate was used on the PUG; the mean muon lifetime is 2.2 μs).

The trigger started a TDC timer, and a signal from any of the positron scintillators stopped it; the time was histogrammed to give **muon decay spectra**. The spectra from the F and B scintillators contained much more noise (due to beam particles) than the U and D scintillators, so U and D data were used for μSR results in this study.

A **"system busy" signal** was formed through a combination of the primary trigger and a "computer busy" signal exerted through a CAMAC. A pulser was used to measure the fraction of time the busy signal was on, although part way through the run this circuit was lost due to a hardware failure.

The T1 ion chamber emits pulses at a rate proportional to the BL1A proton beam current, as described in section 4.1.1. The signal from this chamber was put into a scaler, in an attempt to record the integrated proton beam current and normalize different runs for proper comparison. However, it was later determined to be an unreliable measure of current in some cases, due to changes in the beamline settings; see section 7.7.1.

LeCroy 4208 TDC	
Mean peak spacing:	158.9868 channels
Std. Dev. of spacing:	2×10^{-4} channels
Max. deviation from mean:	6×10^{-4} channels
LeCroy 2228A TDC	
Mean peak spacing:	102.06 channels
Std. Dev. of spacing:	0.25 channels
Max. deviation from mean:	0.94 channels

Table 6.2: Statistics on inter-peak spacings for Time Calibrator Histograms (figure 6.2).

6.3 Data Taking

6.3.1 Production Target

Most data was taken using the beryllium 1AT1 target (which has a stainless-steel water jacket for cooling). Towards the end of the study, the 1AT1 target was switched to a graphite one (with no jacket); this is the type of target *TWIST* will likely use. The muon rates are higher when using the graphite target than with the beryllium target (figure 4.2), but there was no detectable difference in muon polarization.

6.3.2 TDC Calibration

Three methods were used to check the consistency of the TDC's: a random trigger, a Time Calibrator, and the cyclotron period.

Time Calibrator

A Time Calibrator is a device which generates pulses at randomly-chosen intervals to start and stop the TDC; each interval is some integer multiple of a dial setting (the "period", eg. 160 ns).

An Ortec model 462 Time Calibrator was used to calibrate the TDC's (LeCroy 4208 and 2228A model TDC's). Figure 6.2 (a) shows a histogram of the TDC data collected by the 4208 (which was used for the muon decay timing), with the Time Calibrator period set to 160 ns. Figure 6.2 (b) shows the same histogram for the 2228a (which was used for time-of-flight measurements), with the Time Calibrator period set to 10 ns. The exact period of the Time Calibrator cannot be set very precisely, but once set it is very stable.

The number of bins between each pair of peaks was calculated for both TDC histograms, and average spacings were calculated. See table 6.2 for the statistics on these spacings. The "residuals" of the peak spacings were also calculated for each peak pair (that is, (residual) = (spacing between peak pair) - (mean spacing)), and were plotted in figure 6.3.

These results indicate that the measurement precision of the **LeCroy 4208 TDC** is much smaller than one channel; the measurement precision of the **LeCroy 2228A TDC**

(a) 4208 TDC

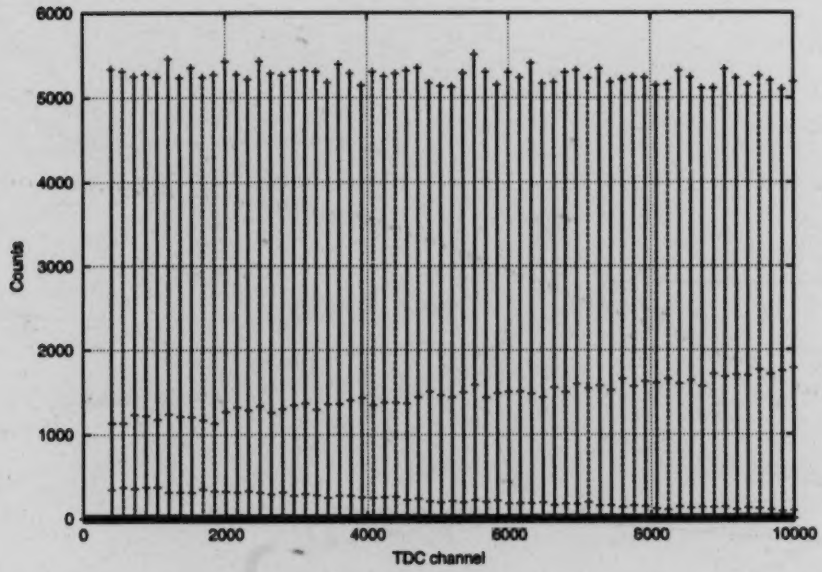

(b) 2228A TDC

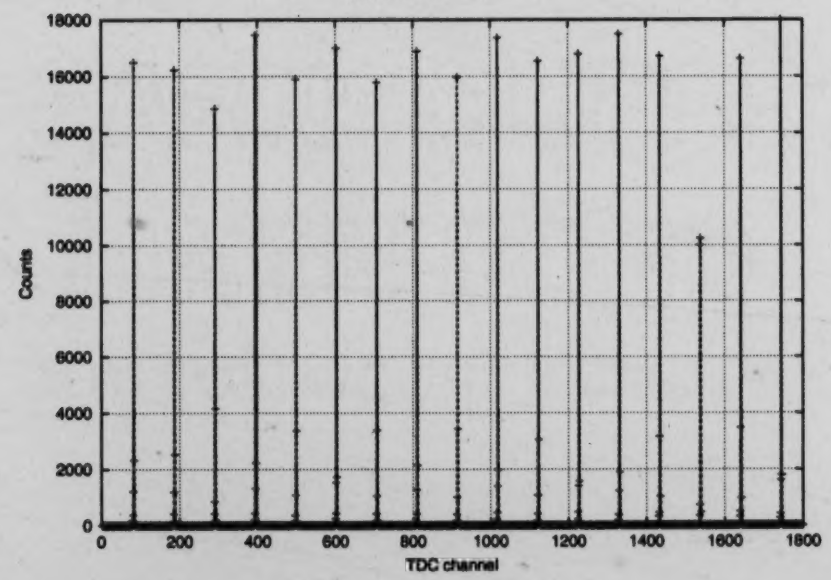

Figure 6.2: Histogram of measurements taken using a Time Calibrator, for LeCroy 4208 (fig. a) and 2228A (fig. b) TDC's.

(a) 4208 TDC

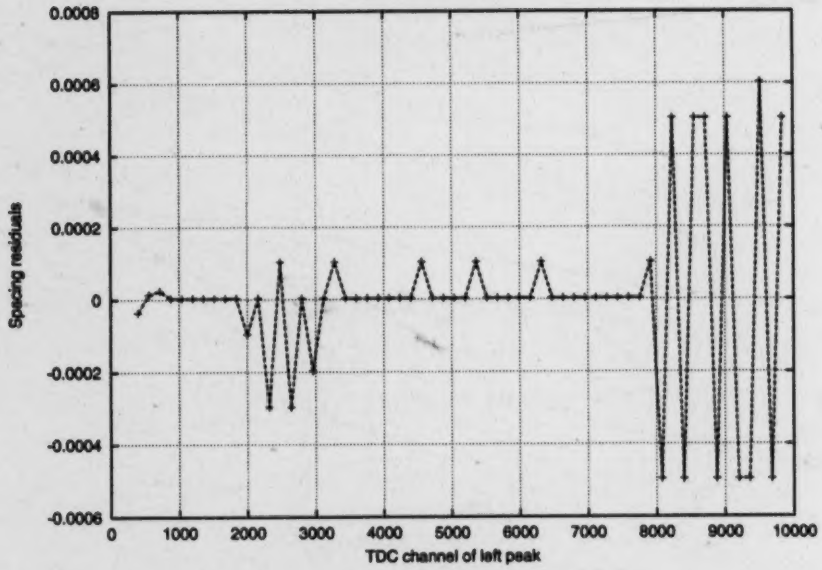

(b) 2228A TDC

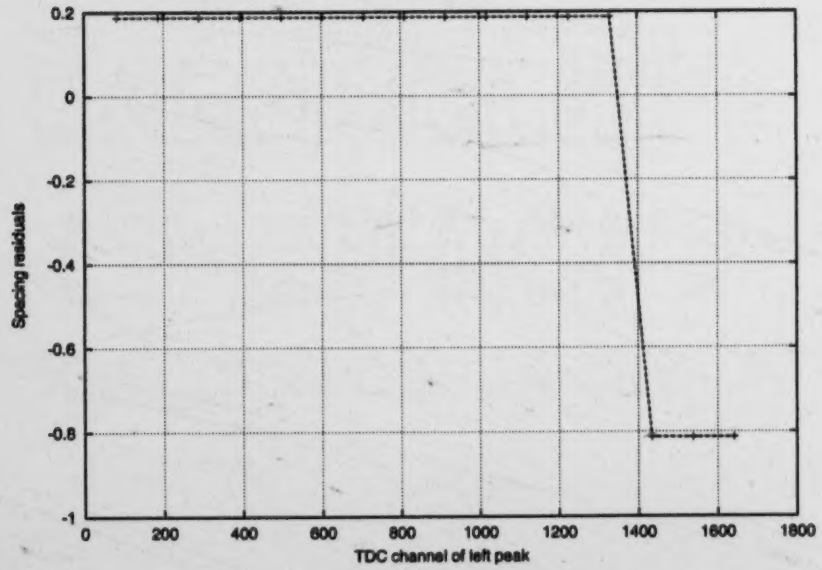

Figure 6.3: "Residuals" (spacing - mean spacing) measured for 4208 TDC (fig. a) and 2228A TDC (fig. b).

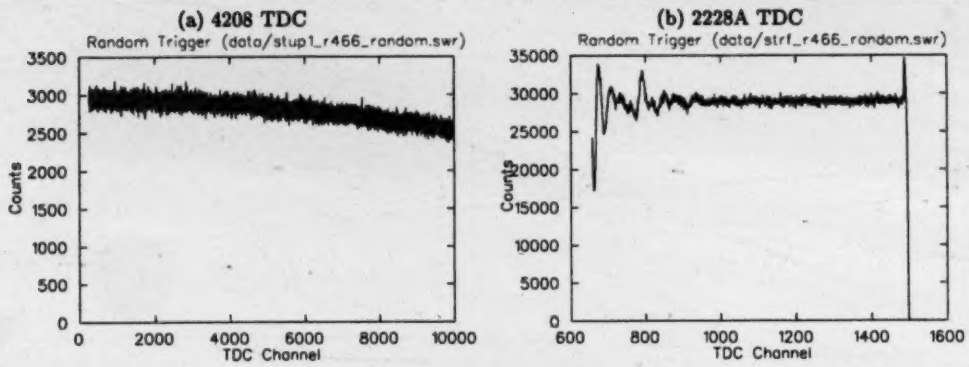

Figure 6.4: Result of a random trigger on the LeCroy 4208 TDC (fig. a) and 2228A TDC (fig. b).

is ±0.25 channels.

Random Trigger

The random trigger was supplied by an additional scintillator and a radioactive source; a pulser was connected to the U and D scintillator electronics to simulate positron signals uncorrelated to the trigger. The resulting histograms are shown in figure 6.4. (Note that the ranges shown on the graph were the only ones used for analysis.)

The response of the 4208 to the random trigger (figure 6.4(a)) slopes downward. This is suspected to be caused by the Pile-Up Gate rejecting data at higher "decay times"—a longer decay time means more opportunity for a pile-up event (a second trigger before the TDC stop pulse) to occur—rather than by a non-uniformity of the TDC itself. The event rate was much higher than that during normal data-taking.

The response of the 2228A (figure 6.4(a)) has wild oscillations in the first half of the graph, but seems flat in the second half. This is believed to be a property of the TDC itself, as the same behaviour is seen in real data (see, for example, figure 7.1). For any analysis requiring good knowledge of the time of flight (which was measured by the 2228A TDC), only the second half of this range was used.

Cyclotron Period

The LeCroy 2228A TDC used to measure time of flight can be calibrated using the cyclotron's period—the time between proton bunches—of 43.38 ± 0.03 ns. Since the particles in the secondary beamlines are created when the protons hit the production target, the structure of these secondary beams (such as M13) repeats every 43.4 ns. To calibrate the number of TDC channels per nanosecond, the number of bins between peaks in the surface muon Time-of-Flight histogram (figure 7.1, page 37) was measured. The peaks were

measured to be 452 channels apart, giving a scale of (43.4 ns/452 ch) = 0.096 ns/ch. The Time-of-Flight axis was rescaled according to this measurement as one of the axis corrections described in section 7.2.2.

(No such calibration was available for the LeCroy 4208 TDC used to measure muon decay time. However, the muon lifetime from μSR fits (eg. figure 7.10) is consistent with the known lifetime, which suggests such a calibration is not needed.)

Chapter 7

Beam Study Analysis and Results

7.1 Analysis software

Initial data acquisition was done using the Midas data acquisition system [1], configured by Dr. Peter Green.

Preliminary analysis (mainly building histograms of the data) was done using the Nova data analysis system [5], configured by Drs. Peter Green and Glen Marshall and me.

Histograms produced by Nova were analyzed using Physica [3], with the help of Physica programs developed by Drs. Glen Marshall and Peter Green.

7.2 Time-of-Flight Structure of the Beam

7.2.1 Calculating Time of Flight

All quantities in this section are in the Lab Frame unless otherwise noted.

If v is a particle's speed, and $\beta = v/c$, then we can obtain β for a particle from its momentum p and rest mass m as follows:

$$\beta = \frac{pc}{E} = \frac{pc}{\sqrt{p^2c^2 + m^2c^4}} \tag{7.1}$$

where E is the particle's energy. Then the time t it takes for the particle to travel a distance d is simply

$$t = \frac{d}{\beta c} = \frac{d\sqrt{p^2c^2 + m^2c^4}}{pc^2} \tag{7.2}$$

The distance from the 1AT1 production target to the end of the M13 beamline is roughly 9.6 m (see section 4.2).

7.2.2 Time of Flight and Cyclotron Period

As discussed in section 4.1.1, the TRIUMF cyclotron produces protons in bunches, 43.38 ± 0.03 ns apart. All particles which enter the M13 beamline are therefore also produced on a

$\sim$ 43 ns cycle.

A capacitive probe on the 1A proton beamline sends out a pulse to each of the experimental areas whenever a proton bunch passes. This pulse is used for timing the arrival of particles in an experiment. It is referred to herein as the "capacitive probe pulse" or just "CP pulse".

Particles with different masses at the same momentum will take different amounts of time to travel the length of the beamline, and so will arrive at the end of the beamline at different times relative to the capacitive probe pulse. The difference between arrival time and the next CP pulse is called the **CP Time-of-Flight** or **CP TOF**.

The circuit used to measure the CP TOF worked as follows: The system trigger started the timer on the LeCroy 2228A TDC. The next capacitive probe pulse was used to stop the timer. (Only every second CP pulse was used, giving two CP cycles in the histogram.) The resulting time is the CP TOF. Because the capacitive probe pulse was used for the stop and not the start of the timer, a longer CP TOF means earlier arrival time—that is, raw CP TOF histograms will appear to have the time axis reversed.

A variable delay line was placed in the CP pulse circuit, to adjust the "phase" of the CP TOF spectra. Because of concerns about the edges of the spectrum (the histogram was observed to have some rise time and fall time at the edges, rather than perfectly sharp, indicating time jitter or some other effect; in addition, data loss was seen at the edges of the histogram), it was useful to adjust the phase to keep the various peaks of the spectra away from the edges. The delay was recorded for each data run, so that all data could later be adjusted to the same phase for comparison.

For a more detailed discussion of particle types and their production, see chapter 4.

Note: Unless otherwise noted, all TDC graphs include a cut on the beam (C) scintillator ADC to remove all signals below 300 channels. This removed most of the beam positrons from the analysis. See section 7.3.2 for details.

7.2.3 Time-of-Flight Structure at Surface Muon Momenta

Surface muons come from pions decaying at rest in the 1AT1 production target (section 4.3.2). The maximum possible momentum for these muons is 29.79 MeV/c, which corresponds to pions decaying right at the target surface without losing energy passing through target material. Momenta below this cutoff (the "surface muon edge") are referred to as surface muon momenta, because muons from the surface (or near the surface) of the 1AT1 target are only available at these momenta. Momenta above this cutoff are referred to as cloud muon mometa, because cloud muons are the only ones available.

The pion lifetime is about 26 ns, comparable to the $\sim$ 43 ns cyclotron period, so surface muons aren't confined to a narrow band in the CP TOF. The pion decay curve is clear in

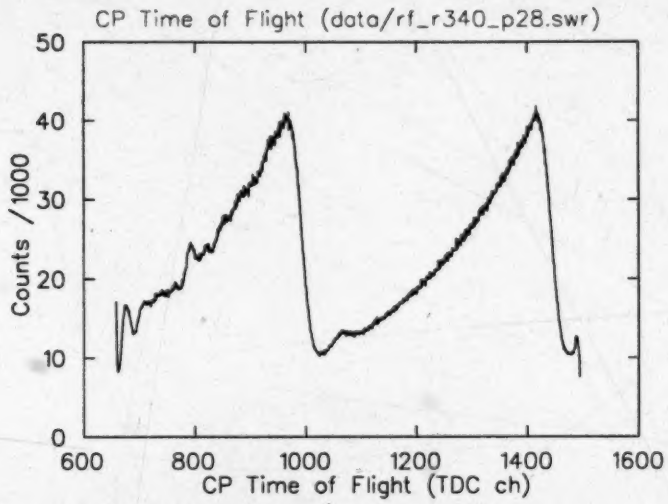

Figure 7.1: Raw CP Time-of-Flight histogram for surface muons (29.2 MeV/c). Horizontal axis is in TDC channels (0.1 ns/channel).

figure 7.2.

Figure 7.1 shows what a "raw" CP TOF histogram looks like (with only the relevant TDC range displayed). Figure 7.2 shows the same histogram with the axis corrections made: the CP axis has been reversed and converted into ns (from TDC channels), and the resulting CP values have been offset by the setting of the variable delay box. (For more convenient comparison, the origin has been marked with a vertical dashed line in most graphs.) This allows for a consistent comparison of the data from different runs which may have used different delay settings. The data for these figures was taken at 29.2 MeV/c.

The oscillations in the first half of figure 7.1 are due to non-linearities in the TDC itself (see section 6.3.2), and exist in all CP TOF graphs. For this reason, most analysis requiring careful CP TOF measurements used only the second half of these graphs.

The exponential decay curve is obvious in figure 7.2, indicating that the data is dominated by surface muons, as expected. The small peak at the base of the decay curve (near 30 ns in this figure) is due to pions, as shown in section 7.3.1.

All CP Time-of-Flight histograms herein will be shown with axis corrections in place, unless otherwise noted.

The CP TOF spectrum for 26.3 MeV/c (10% below the momentum used for figure 7.2 and well below the surface muon edge) is shown in figure 7.3, after CP axis corrections. The structure is the same as in figure 7.2, but shifted due to the lower momentum. The muons shift by about 12 ns with respect to the origin, in agreement with the shift predicted by equation 7.2.

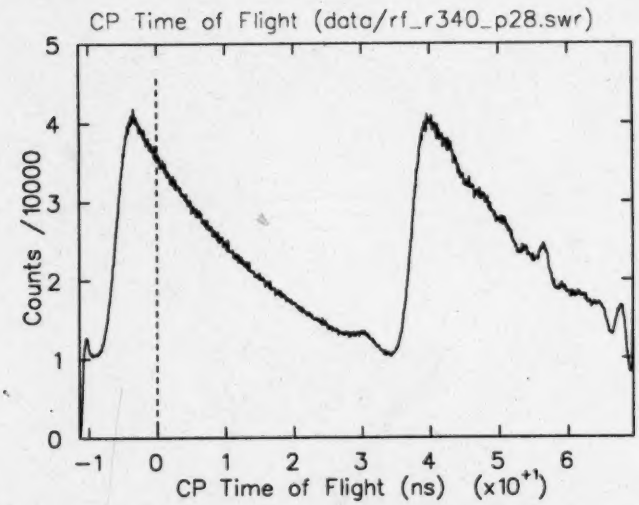

Figure 7.2: CP Time-of-Flight histogram for surface muons (29.2 MeV/c), with corrections to the CP axis.

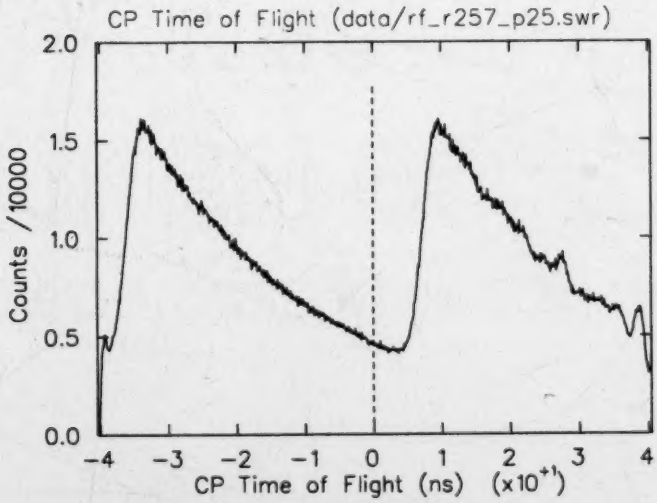

Figure 7.3: CP Time-of-Flight histogram for surface muons (26.3 MeV/c, 10% below the momentum in figure 7.2), with corrections to the CP axis.

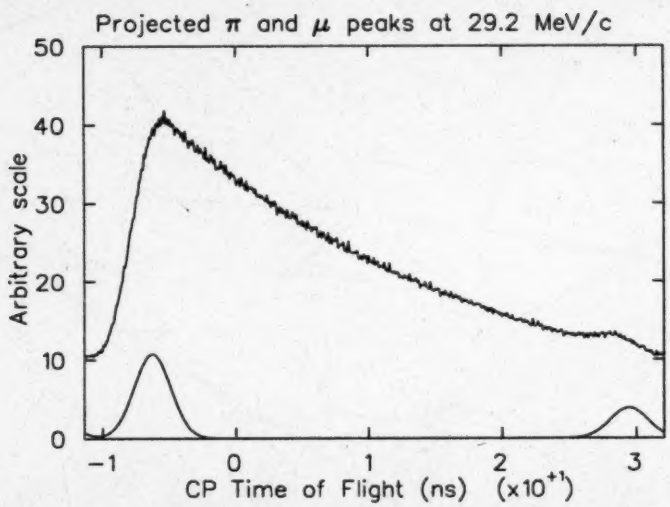

Figure 7.4: Estimated locations of pion and cloud muon peaks at 29.2 MeV/c (based on Time-of-Flight), overlaid on actual CP TOF distribution. Projected peak sizes are representative of rates calculated in section 7.7. The larger peak is cloud muons, the smaller pions.

Using equation 7.2 to determine the difference in travel times for 29.2 and 32.1 MeV/c, we can estimate where the pion and cloud muon peaks should be in this figure based on where they occur at 32.1 MeV/c (figure 7.5). These peaks are shown in figure 7.4, overlaid on the CP TOF distribution for 29.2 MeV/c. Cloud muons are prompt as they arise from pions decaying in flight near the production target. Therefore, they arrive at the detector in time with the surface muons from prompt pion decay.

The pion and cloud muon peak positions can be further projected to 26.3 MeV/c. As mentioned above, the change in time of flight for muons between 29.2 MeV/c and 26.3 MeV/c is about 12 ns; for pions the change is about 16 ns. This puts the pion peak in about the same CP TOF region as the cloud muons, because of the 43 ns "wrap-around" in the measurement.

7.2.4 Time-of-Flight Structure at Cloud Muon Momenta

Cloud muons come from pions decaying in flight, near the 1AT1 production target or somewhere within the M13 beamline (section 4.3.3). As a result, only the fastest-decaying pions produce cloud muons (other pions leave the area; their decay products are not aligned to enter the beam channel). This means the cloud muons will appear in a narrow peak, similar in shape to the pion peak, in a CP Time-of-Flight histogram.

Cloud muons can occur at any momentum, but are much easier to see at momenta above 29.79 MeV/c (the surface muon edge). At low momentum, the surface muon rate is much

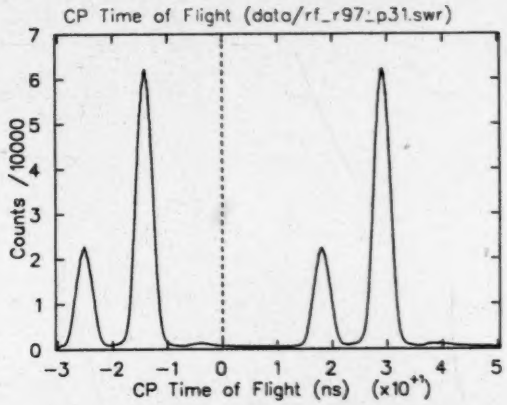

Figure 7.5: CP Time-of-Flight histogram for cloud muons (32.1 MeV/c), with corrections to the CP axis.

higher than the cloud muon rate.

Figure 7.5 shows a CP TOF histogram taken at 32.1 MeV/c, with corrections (phase, etc.) made to the CP axis. The oscillations mentioned in section 7.2.3 are not obvious here because they occur in the low, flat part of the histogram (around 40–50 ns).

The largest peaks (at about −15 and +30 ns in figure 7.5) are due to cloud muons. The other large peaks (near −25 and +20 ns) are due to pions. A very small peak is visible between −10 and 0 ns, and again between +35 and +45 ns; these peaks are due to positrons. There is also a barely visible continuous positron background. Although there are many more positrons in the beam than any other particle (section 7.7), they leave very little energy in the thin beam counter (the C scintillator), as they are minimum-ionizing particles at this momentum. We were therefore able to remove most of the positrons from the trigger using a cut on the energy deposited in the C scintillator (measured by the C scintillator discriminator and by an ADC).

7.3 Particle Identification

Because of the energies involved, the only particles expected to be seen in the beam are positrons, muons, and pions. Any protons in the beam will be unable to even penetrate the mylar vacuum window at the end of the M13 beam pipe.

7.3.1 Time of Flight

One method of particle identification is to change channel momentum and see how much each particle's time of flight changes.

Compare the two graphs in figure 7.6, taken at momenta of 32.1 and 35.0 MeV/c. Using

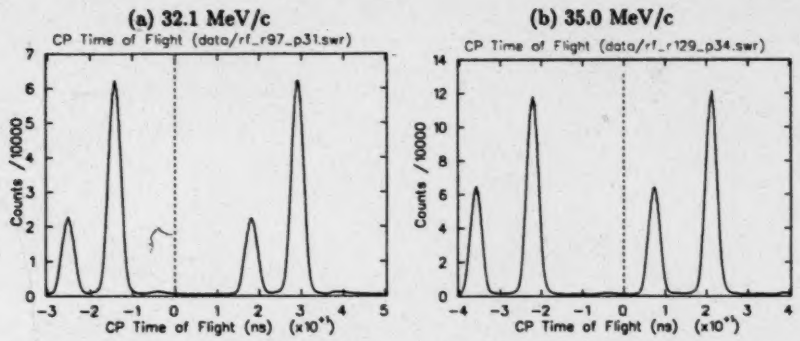
(a) 32.1 MeV/c
CP Time of Flight (data/rf_r97_p31.swr)
Counts /10000
CP Time of Flight (ns) (x10⁻⁹)
(b) 35.0 MeV/c
CP Time of Flight (data/rf_r129_p34.swr)
Counts /10000
CP Time of Flight (ns) (x10⁻⁹)

Figure 7.6: CP TOF histograms for cloud muons, at 32.1 (fig. a) and 35.0 MeV/c (fig. b).

equation 7.2 to estimate the travel times and determine the CP TOF shift Δt for each type of particle, between momenta of 32.1 and 35.0 MeV/c, gives $\Delta t_\pi = 11.8$ ns, $\Delta t_\mu = 8.5$ ns, and $\Delta t_e = 0.0$ ns. In the graphs, the largest peak shifts by about 7.5 ns, the smaller peak shifts by about 10.5 ns, and the very small peak between -10 and 0 ns does not move at all (relative to the origin); this suggests that the peaks are due, in order of decreasing peak size, to muons, pions, and positrons. The discrepancies are probably due to inaccuracies in the CP phase corrections, or errors in the particle flight path length.

7.3.2 Beam Scintillator ADC

Particles moving at higher speed tend to deposit less energy when passing through material[1]; at a given momentum, heavier particles will be moving more slowly and will therefore deposit more energy. An ADC measuring the pulse height of the beam (C) scintillator signals can be used to distinguish between muons and pions, and confirm the identifications made with time-of-flight data.

Figure 7.7 shows the ADC histogram for the C scintillator, at 32.1 MeV/c. The small peak on the left is due to the tail of the positron distribution, cut off by the discriminator threshold. The rest of the distribution is due to muons and pions, although it is difficult to tell that two different particle types are present.

Figure 7.8 more clearly shows the different particles: two peaks are visible, with different pulse heights and different CP TOF times, as well as a band below 200 ADC channels which represents the positron background. (A cut placed at 300 ADC channels will remove almost all of the beam positrons while keeping the muons and pions. For this reason, histograms of TDC data (such as CP TOF graphs or muon decay histograms) have this cut in place.) The peaks around -25 and $+20$ ns CP are due to particles which left much more energy

[1]This is only true for particles travelling at much less than the speed of light; as a particle's energy becomes high enough (GeV), the energy deposited passes through a minimum and rises again. This is known as the "relativistic rise."

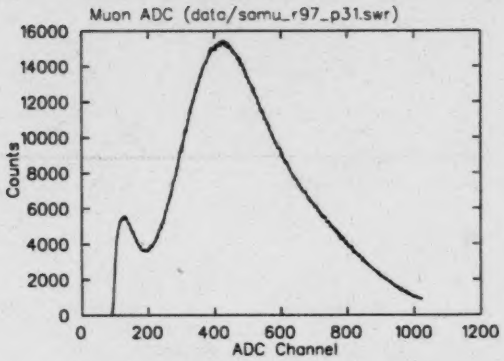

Figure 7.7: Histogram of ADC data for beam (C) scintillator, 32.1 MeV/c.

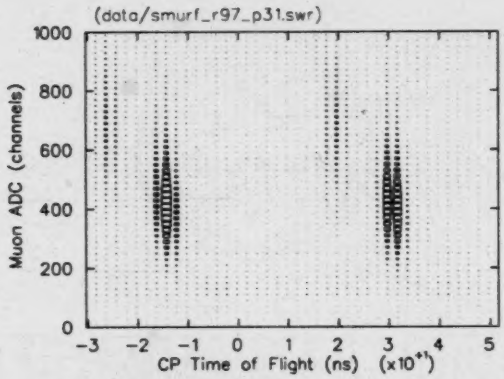

Figure 7.8: 2D histogram of C scintillator ADC signal vs. CP TOF, 32.1 MeV/c.

in the C scintillator than those at -15 and $+30$ ns CP, which suggests that the former are the pions and the latter are the muons. This is consistent with the peak identification in section 7.3.1.

7.4 Polarization Measurements

The majority of this beam study was performed using a beryllium production target (with a steel water jacket) at 1AT1 (see section 4.3.1), so the results quoted will be those of the beryllium target unless otherwise noted. Some data was taken using a carbon 1AT1 production target to confirm the results, particularly the polarization results; the carbon target results are quoted at the ends of sections 7.4.1 and 7.4.2. All carbon target results were consistent with the beryllium target results.

As discussed in chapter 5, the decay spectrum for a muon precessing in a magnetic field

is described by

$$N = N_0 e^{-t/\tau}(1 + \alpha \cos(2\pi f t + \phi)) + B \tag{7.3}$$

where N = counts, t = decay lifetime, N_0 = normalization, τ = lifetime, α = asymmetry, f = precession frequency, ϕ = precession phase, and B = constant background.

The asymmetry parameter α is directly proportional to the muon polarization P_μ. If we assume that the polarization of the surface muons is exactly -1 (which should be true to the level of precision of this beam study), then the ratio of a particle's asymmetry relative to the surface muon asymmetry α_s gives us that particle's polarization. (eg. The polarization of cloud muons, P_c, is given by $P_c = \alpha_c/\alpha_s$.)

There is some redundancy between the value of ϕ and the sign of α: changing ϕ by $\pm\pi$ reverses the sign of α. For this study, I have chosen to keep $0 \leq \phi < \pi$ and let the sign of α define the polarization direction. Furthermore, I have chosen α_s (the surface muon asymmetry) to be defined as positive. Note that, by physical arguments, the actual direction of the surface muon polarization is opposite the beam direction, so particles with $\alpha < 0$ are polarized in the beam direction.

The phase ϕ has two components. Since the start of each μSR spectrum is clipped off (to remove the effects of time jitter, etc.) the position of the origin is arbitrary; this results in an offset to the phase. For this analysis, the origin was kept to the same position for all μSR spectra, so this offset should not change between data sets. Relative phases between particles are more important, as they indicate a real difference in the direction of polarization; cloud and surface muons are expected to have the same phase (with the sign of α denoting differences of π), by geometrical symmetry. The phase for muons from stopped pion decay in the apparatus (see section 7.4.1) depends entirely on apparatus geometry, since the pion decay itself is isotropic.

As described in section 7.3.1, CP Time-of-Flight can be used to identify particles. Separating the data from the U or D scintillators by CP TOF allows the measurement of the polarization of different particle types separately.

Since the composition of the beam varies with CP Time-of-Flight, and many of these measurements were desired with various subsections of the CP TOF distributions, most measurements were made using projections of 2-dimensional histograms of decay time vs. CP TOF. The desired CP TOF ranges were selected from these histograms and projected onto the decay time axis. These projections are what were used for the μSR fits.

Figure 7.9 shows the decay time vs. CP TOF histograms for the D ("Down" scintillator) TDC, at 29.2 and 32.1 MeV/c.

Table 7.1 summarizes the results of this beam study. It includes the asymmetry for each of the particles, and what polarization those correspond to; as mentioned, polarization is given by $P_i = \alpha_i/\alpha_s$, and the uncertainty δP_i takes both $\delta\alpha_i$ and $\delta\alpha_s$ into account. Sections

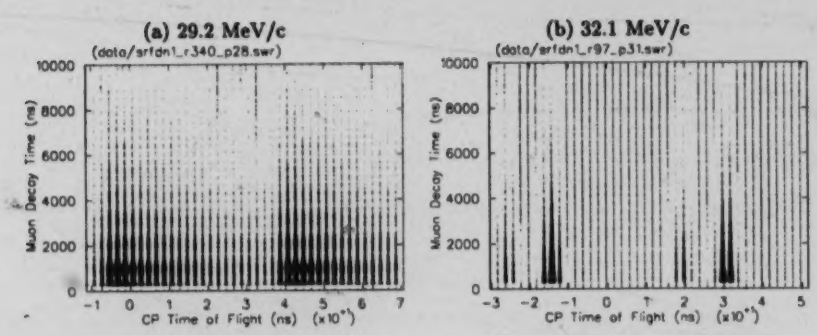

Figure 7.9: Histograms of Decay time vs. CP Time-of-Flight, D scintillator, at 29.2 MeV/c (a) and 32.1 MeV/c (b).

		Asymmetry α	Polarization P
Surface muons	U	$\alpha_s = 0.253 \pm 0.002$	
(29.2 MeV/c)	D	$\alpha_s = 0.241 \pm 0.002$	
Cloud muons	U	$\alpha_c = -0.085 \pm 0.004$	$P_c = 0.34 \pm 0.05$
(32.1 MeV/c)	D	$\alpha_c = -0.072 \pm 0.004$	$P_c = 0.30 \pm 0.02$
Pions	U	$\alpha_\pi = 0.060 \pm 0.007$	$P_\pi = -0.2 \pm 0.1$
(32.1 MeV/c)	D	$\alpha_\pi = 0.033 \pm 0.006$	$P_\pi = -0.14 \pm 0.03$

Table 7.1: Summary of relative polarizations for various beam particles. Polarizations are relative to surface muons.

7.4.1 and 7.4.2 discuss the asymmetry and polarization results in more detail.

The "polarization" value of pions is due to the muons from pions which decay within the detector. See section 7.4.1 for details.

7.4.1 Beam Polarization at Cloud Muon Momenta

As shown in figure 7.9(b), selecting either cloud muons or pions for a μSR fit, at $p >$ 29.79 MeV/c, is a simple matter of making a cut on CP TOF; this gives an almost completely uncontaminated signal. (The only contamination should be beam positrons, most of which were removed by the ADC cut on the C scintillator. In a μSR context, beam positrons should only contribute to the constant background.)

Beryllium Target Results

Selecting one of the two cloud muon peaks from the D scintillator data and fitting the μSR function to it shows that the **cloud muon asymmetry** is $\alpha_c = -0.072 \pm 0.004$ for this geometry. Comparing this to the surface muon results (section 7.4.2) to determine polarization, we see that the direction is opposite and the magnitude is $|P_c| = |\alpha_c/\alpha_s| = 0.30 \pm 0.02$ relative to surface muons. See figure 7.10 for the decay spectrum and the fitted

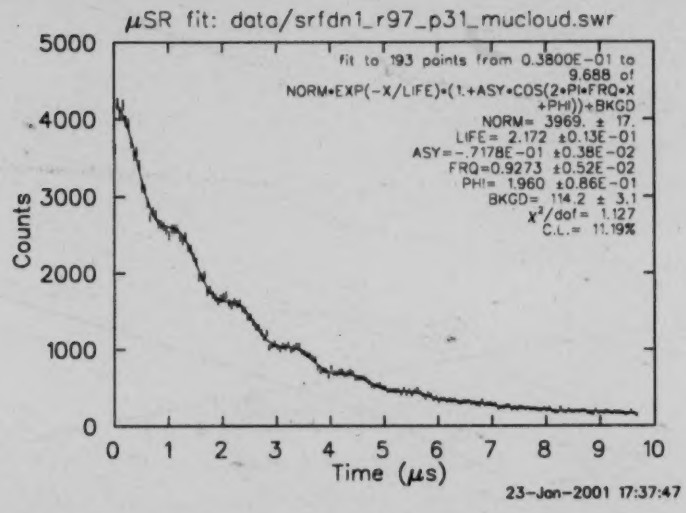

Figure 7.10: Cloud muon decay spectrum (32.1 MeV/c data), and μSR fit function. Error bars are statistical.

curve. U scintillator data produces results consistent with these.

The phase ϕ is close to that measured for surface muons (figure 7.14): the difference is $|\phi_c - \phi_s| = |(1.96 \pm 0.09) - (1.62 \pm 0.01)| = 0.3 \pm 0.1$, which is within three standard errors of zero.

The poor χ^2/dof (χ^2 per degree of freedom) shown in the plot is most likely due to an underestimate of the uncertainties; the only errors included in the data are statistical.

The same process was followed to perform a μSR fit to the cloud muon decay spectrum at 35.0 MeV/c; see figure 7.11 for the decay spectrum and the fitted curve. This fit gave a cloud muon asymmetry of $\alpha_c = -0.067 \pm 0.003$, which is consistent with the 32.1 MeV/c result above. Muon lifetime τ, precession frequency f, and precession phase ϕ also agreed within error between the 32.1 and 35.0 MeV/c data.

Pions decay into muons, of course, and for geometrical reasons the muons they produce appear polarized. Obviously, this polarization depends entirely on the detector, as the pion decay itself is isotropic. In the case of this beam study, for example, the pion stopping distribution is not uniform through the aluminum target. (Even at 35 MeV/c, the pions are estimated to stop only 0.4 mm into the aluminum target.) Since the U and D scintillators are on opposite sides of the target, it is not surprising to see different asymmetry values for the decay spectra from these scintillators. Figures 7.12(a) and (b) show the decay spectra for pion data as recorded by the U and D scintillators, as well as their μSR fits.

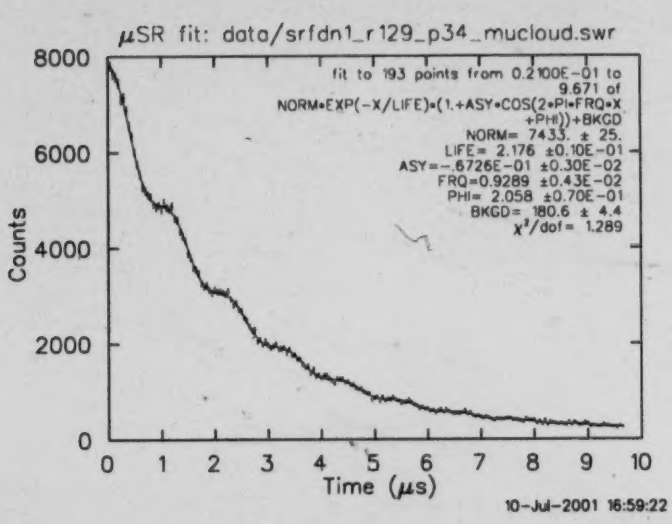

Figure 7.11: Cloud muon decay spectrum (35.0 MeV/c data), and μSR fit function. Error bars are statistical.

Carbon Target Results

The asymmetry measured for cloud muons using a carbon production target (section 4.3.1) and the D scintillator data was $\alpha_c = -0.068 \pm 0.002$, consistent with the value from the beryllium target.

The μSR phase was measured to be $\phi_c = 1.79 \pm 0.04$, consistent (within two standard errors) with the value from the beryllium target. It is within three standard errors of the phases measured for surface muons in both target types.

7.4.2 Beam Polarization at Surface Muon Momenta

As shown in figure 7.2, the surface muons completely swamp out the pion and cloud muon peaks in the 29.2 MeV/c CP Time-of-Flight spectrum. However, cloud muons are present, and have a significant impact on the beam polarization.

Beryllium Target Results

A μSR fit was applied to the decay time spectrum defined by each CP bin in figure 7.13(a), over roughly the portion of the plot with CP Time-of-Flight $\lesssim 30$ ns (the first half of the graph; the second half suffered from a hardware fault (fig. 7.2)). Figure 7.13 shows the normalization (proportional to the number of counts in that CP bin) and asymmetry values found by the fits to those CP bins. The CP offset has been adjusted to place the lowest bin at the origin, for convenience.

Two dips in the asymmetry value (and hence in beam polarization) are visible in figure

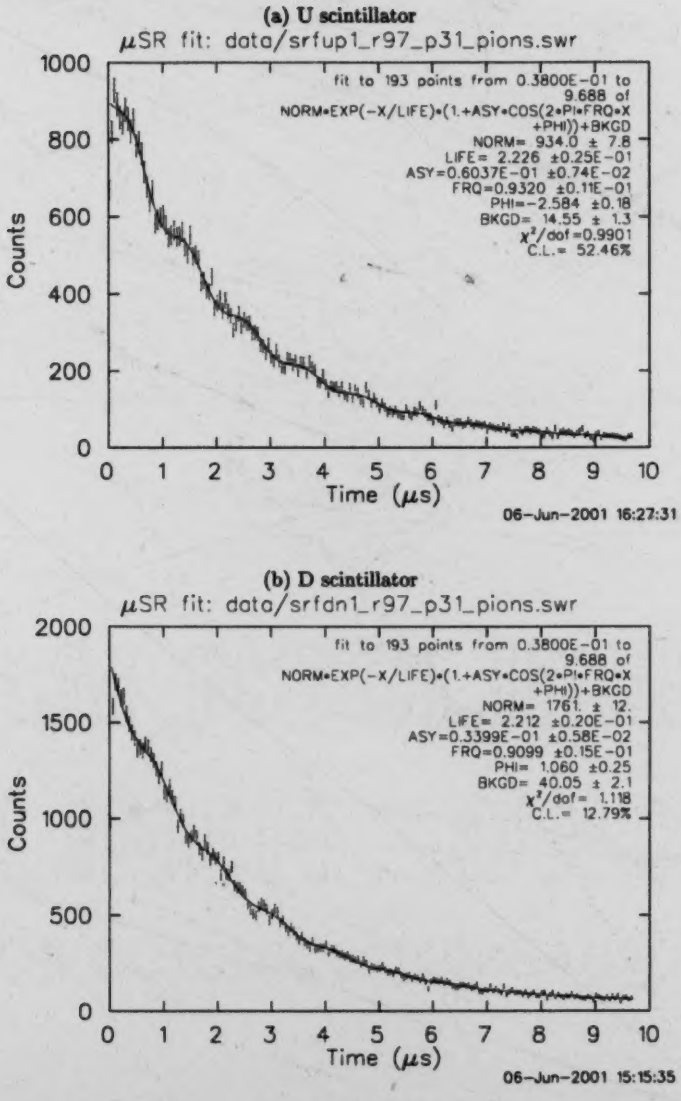

Figure 7.12: Muon decay spectra for 32.1 MeV/c pion data, with μSR fits. Spectrum (a) is from the U scintillator data, and (b) is from the D scintillator.

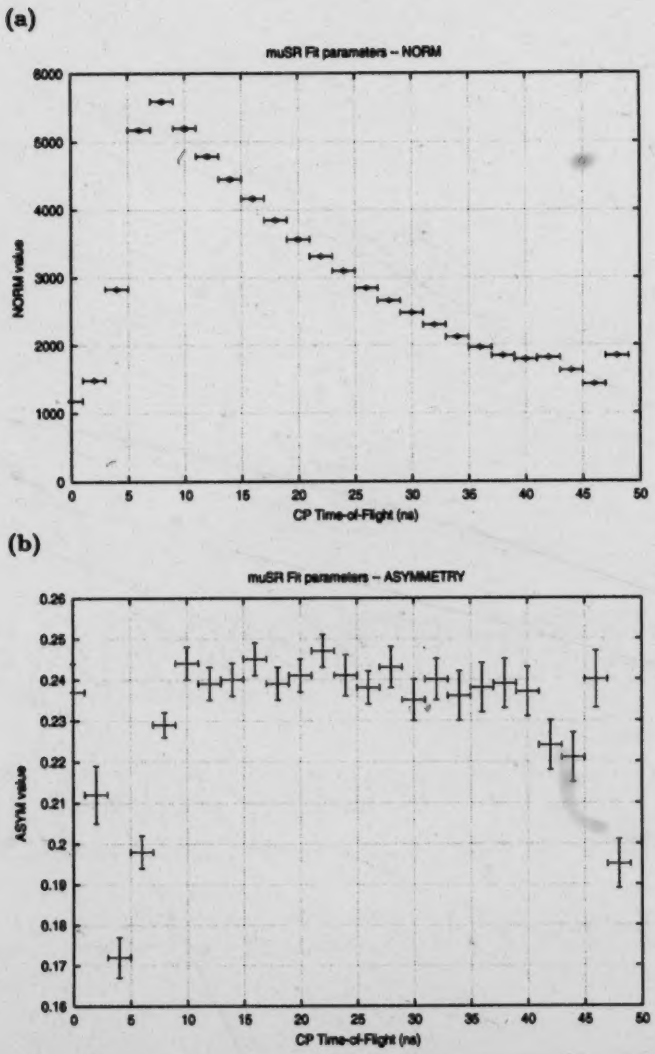

Figure 7.13: μSR fit parameters vs. CP Time-of-Flight, 29.2 MeV/c, D scintillator data. Fig. (a) shows the normalization N, and Fig. (b) shows the asymmetry α.

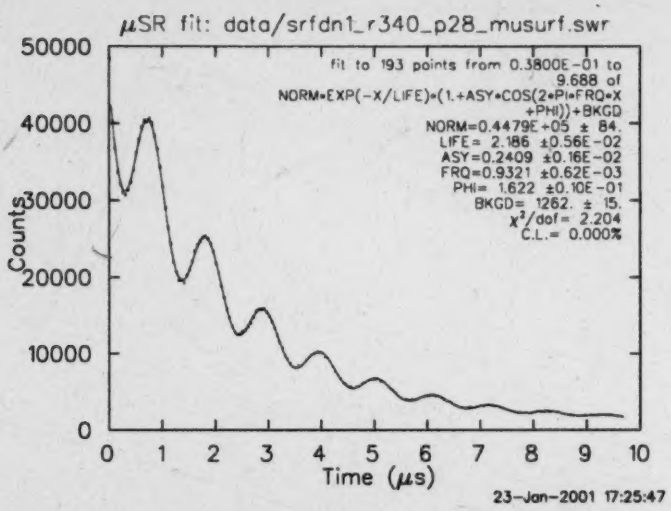

Figure 7.14: Surface muon decay spectrum (29.2 MeV/c data), and μSR fit function. Error bars are statistical.

7.13(b), one around a CP of 5 ns (on this CP scale), and a smaller one between 40 and 45 ns.

Comparing figures 7.4 and 7.13, it's clear that the dips in asymmetry coincide with the presence of cloud muons or pions in the beam. This is consistent with the discussion of section 7.4.1.

Figure 7.13(b) defines a "window" of uncontaminated surface muons, between about 10 and 40 ns in this plot. Combining this data set and fitting the μSR function to it shows that the **surface muon asymmetry** is $\alpha_s = 0.241 \pm 0.002$ in this apparatus (D scintillator); see figure 7.14 for the decay spectrum and the fitted curve. Similar measurements using U scintillator data (not graphed) give $\alpha_s = 0.253 \pm 0.002$; one difference between the two data sets is that they are on opposite sides of the aluminum stopping target.

The process used to produce figure 7.13 was followed using 26.3 MeV/c data to produce figure 7.15. Only one dip in the asymmetry value is really evident; this dip is in the rising edge of the surface muon distribution, ie. where the cloud muons are. (The dip at the far right edge of the plot is in the rising edge of the next CP cycle.) The asymmetry is within error of being constant for the rest of the CP distribution; this is consistent with the prediction that the pion and cloud muon peaks coincide, as well as with the prediction that the pion rate is extremely low.

Fitting the μSR function to the D scintillator data with CP TOF values in the "flat" region of figure 7.15 gives an asymmetry value of $\alpha_s = 0.235 \pm 0.004$, which is consistent with the value $\alpha_s = 0.241 \pm 0.002$ measured at 29.2 MeV/c.

(a)

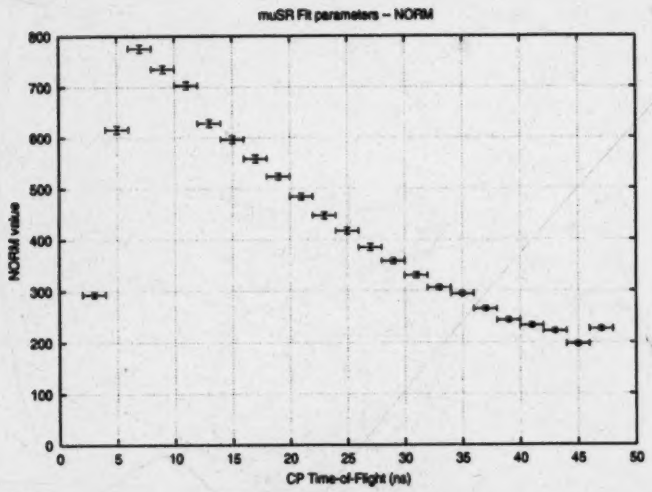

(b)

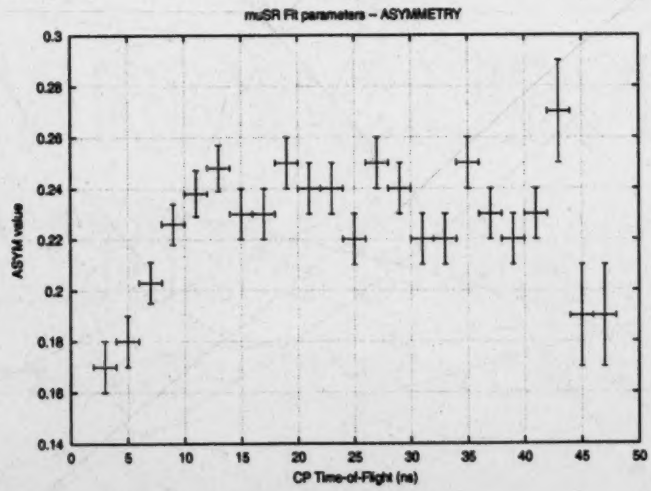

Figure 7.15: μSR fit parameters vs. CP Time-of-Flight, 26.3 MeV/c. Fig. (a) shows the normalization N, and Fig. (b) shows the asymmetry α.

Carbon Target Results

A similar procedure was used to select surface muons using a CP TOF cut.

The asymmetry measured for surface muons using a carbon production target (section 4.3.1) and the D scintillator data was $\alpha_s = 0.238 \pm 0.002$, consistent with the value from the beryllium target.

The μSR phase was measured to be $\phi_s = 1.57 \pm 0.01$, consistent within three standard errors with the value from the beryllium target.

7.5 μSR Simulation with GEANT

A simplified version of the μSR apparatus (using only the scintillators and the stopping target) was simulated with version 3.21 of the GEANT Monte Carlo software [6], developed at CERN by the Application Software Group.

The scattering of the muons in air and other materials will reduce their polarization. A GEANT study was conducted to check their polarization upon entering the stopping target, using either air or vacuum to surround the scintillators. As shown in figure 7.16, the polarization is unaffected by the presence of air, to the level of a part in 10^4.

The simulation was also used to produce μSR spectra to compare simulated asymmetries to measured ones. Figure 7.17 shows the μSR spectrum for simulated surface muons, using data from the D scintillator. The measured asymmetry for this data (0.274 ± 0.003) is inconsistent with the measured surface muon asymmetry ($\alpha_s = 0.241 \pm 0.002$).

Since the actual target was not centred in the real μSR apparatus, the GEANT simulation was rerun with the target closer to the actual position; see figure 7.18 for the resulting μSR spectrum. The asymmetry for this run ($\alpha_s = 0.276 \pm 0.003$) is consistent with the centred-target simulation. This indicates low sensitivity to solid angle effects. (The phase ϕ is very different between the two target positions—for the centred target, $\phi = (-2.92 \pm 0.02) = (0.22 \pm 0.02) - 2\pi$, and for the offset target, $\phi = (8.11 \pm 0.02) = (1.83 \pm 0.02) + 2\pi$; ϕ is physically equivalent to $\phi \pm 2\pi$. Moving the stopping position of the target changes the detector geometry, which will change ϕ.)

One possible reason for the discrepancy between simulated and measured surface muon asymmetry is threshold effects. A particle passing through a scintillator must deposit a certain minimum amount of energy in order to pass the discriminator. Since higher energy positrons deposit less energy, the discriminator thresholds may have been cutting out the highest energy positrons, which is where the strongest angular dependence is in the Michel spectrum (see figure 2.1). This could explain why the simulation—which does not include threshold effects—gave a larger asymmetry value than the real measurement. These effects were not investigated further.

(a) Vacuum

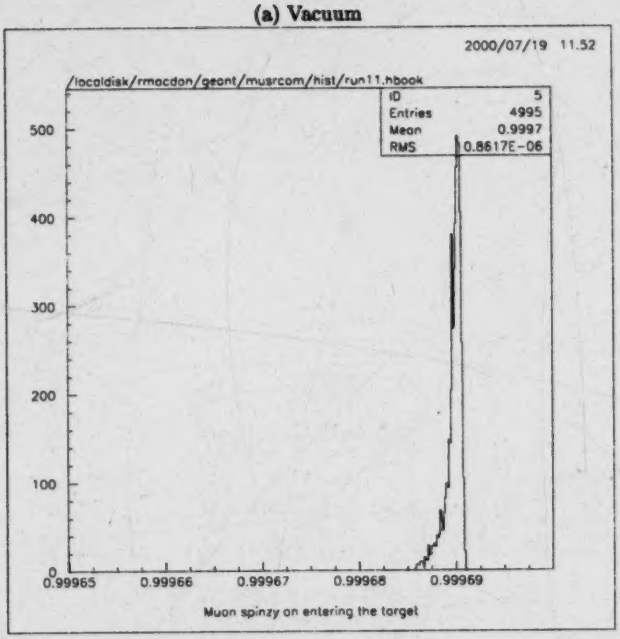

(b) Air

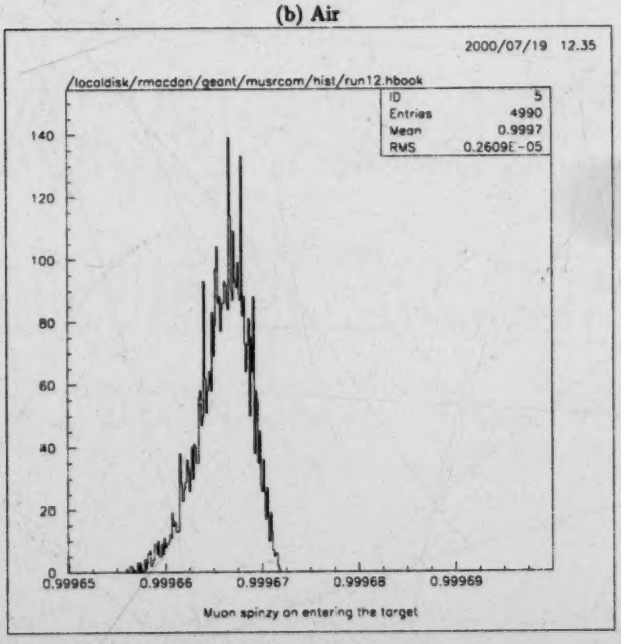

Figure 7.16: Effect of air on muon polarization. Muons pass through beam (C) scintillator (fig. 6.1), then through vacuum (fig. a) or air (fig. b) before reaching the stopping target. Plotted here is the muon polarization (labelled "spinzy" here) upon entering the target.

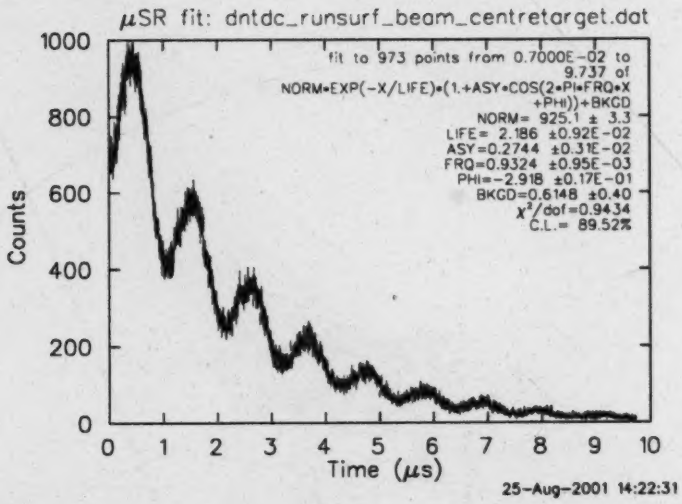

Figure 7.17: μSR spectrum from simulated surface muon data; DOWN TDC data, centred target.

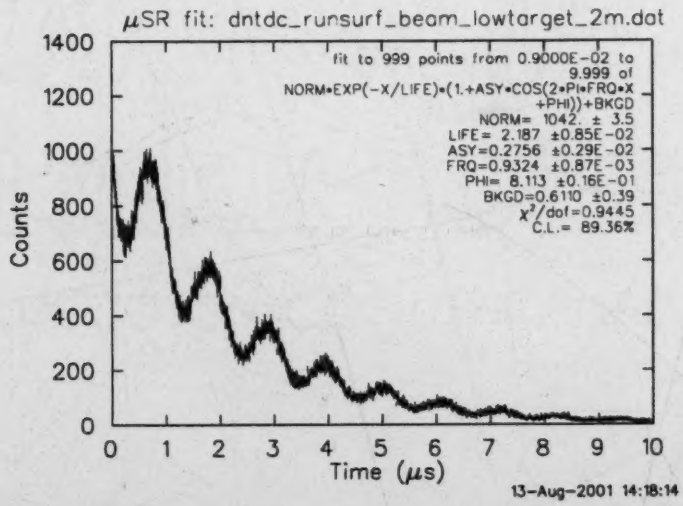

Figure 7.18: μSR spectrum from simulated surface muon data; DOWN TDC data, offset target. (Adding 2π to the phase does not change its physical meaning. Here the function fit converged on $\phi = 8.11$ rather than $\phi = 1.83$.)

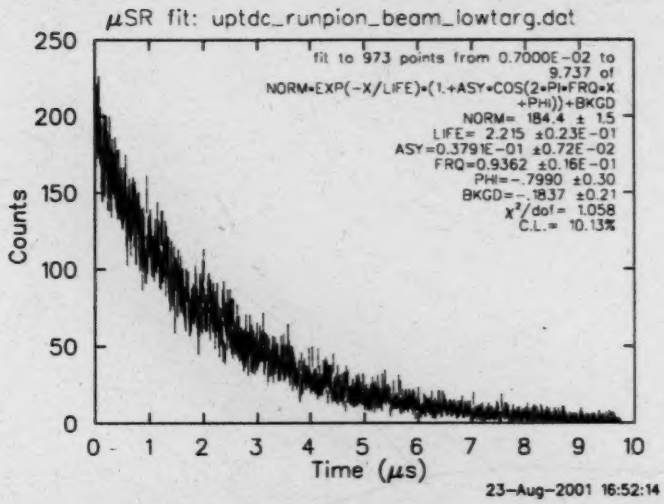

Figure 7.19: μSR spectrum from simulated pion data; UP TDC data, centred target.

When the μSR spectrum for the pion beam was first measured to have a non-zero asymmetry, the μSR GEANT simulation was run with a pure pion beam to confirm the results. This pion beam used the same beam parameters (emittance, momentum, etc.) as the simulated muon beam. Fits were performed for both the U and D scintillator data; the U data is shown in figure 7.19.

A fit could not be calculated for the D scintillator data, but the U scintillator data is shown in figure 7.19 with μSR fit. (These data also used an offset stopping target.) The measured asymmetry is 0.038 ± 0.007 for both TDC's, lower than the measured asymmetry of the pion μSR spectra ($\alpha_\pi = 0.060 \pm 0.007$, section 7.4.1), but comparable to the measured value for the D scintillator. This emphasizes how sensitive the μSR spectrum from a pion beam is to detector geometry. The energy threshold effects described above may also have affected these results.

7.6 Selecting Surface Muons by CP Time-of-Flight

As seen in figure 7.4 (p. 39), a large range of CP Time-of-Flight is essentially pure surface muons. By selecting on this range, we remove most of the contaminating background due to pions or cloud muons. Positrons are removed by a cut on the energy deposited in the beam scintillator.

Gaussian curves were fit to the pion and cloud muon peaks in figure 7.5, and these curves were used to estimate the number of background particles (pions + cloud muons) in each bin of figure 7.13. From this, an estimate can be made of how many background particles

Window width (ns)	B/M	M/M_{tot}
29	6×10^{-4}	0.67
26	2×10^{-5}	0.60
24	$< 1 \times 10^{-5}$	0.55
22	$< 1 \times 10^{-5}$	0.50
20	$< 1 \times 10^{-5}$	0.45

Table 7.2: Background levels for various CP Time-of-Flight cuts. B is the number of background particles (pions and cloud muons) that pass the cut, and M is the number of surface muons. M_{tot} is the total number of surface muons in the beam, before the cut. For the 20, 22, and 24 ns windows, the estimated background rate was negligible.

are in a given CP TOF cut. Table 7.2 lists these estimates for a few sample CP TOF cuts.

As one would expect, there is a tradeoff between supressing background and keeping surface muons. A wider CP TOF cut can be used if the CP TOF positions of the pion and cloud muon peaks are well-known. *TWIST* will be capable of locating the pion and cloud muon peaks at surface muon momenta; see section 3.4.

TWIST can measure the beam polarization as a function of CP TOF to at least the same accuracy as this study[2], which should allow it to determine the CP TOF positions of the pion and cloud muon peaks in the surface muon beam using the technique shown in figure 7.13. Once these positions are known, a CP cut can be selected.

7.7 Particle Rates

7.7.1 Calibrating T1ION Scaler to Proton Beam Current

As discussed in section 4.1.1, the T1ION pulser signal is available; its rate is proportional to the BL1A proton beam current at the 1AT1 target. (It is not perfect, however; it can drift over time, and its response is not entirely linear over a wide range of proton currents. It is assumed good enough for these studies, in general.) Counting the T1ION pulses over time then gives a measure of "integrated current", ie. the number of protons that passed the target in that amount of time.

At the beginning of each run, a visual scaler counted T1ION signals for 10 seconds, then divided by 10 to get a counts/second measurement. At the same time, the BL1A current was noted. The data is plotted in figure 7.20, along with a straight line fit. The calibration function is

$$B = ((2.6 \pm 0.1) \times 10^{-3} \mu\text{A·s/count})T + ((74 \pm 3)\mu\text{A·s}) \qquad (7.4)$$

where B is the integrated BL1A current (in μA·s), and T is the T1ION count.

[2]Measuring the beam polarization to a much higher precision would rely on the very physics that *TWIST* is designed to measure.

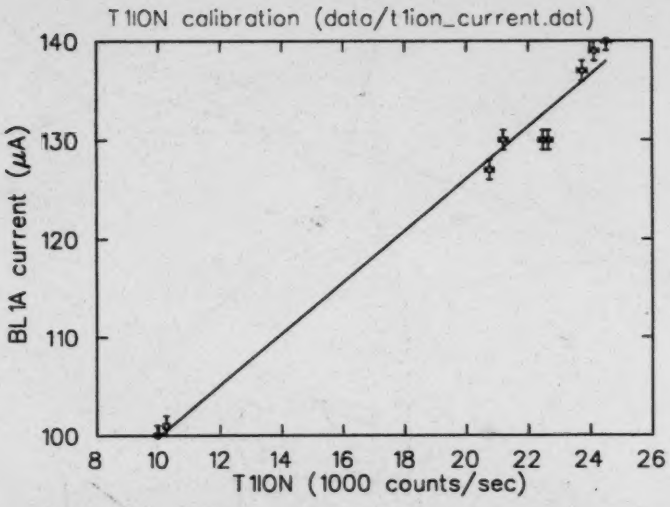

Figure 7.20: Calibration curve: T1ION scaler to integrated BL1A proton beam current. T1ION uncertainties are statistical; BL1A uncertainties are estimated from proton beam current stability (±1 μA·s).

To optimize data acquisition, a trigger rate of about 50000 counts per second was desired (this was about the maximum that the data acquisition system could handle comfortably), and this rate was achieved by the manipulation of the slits ("F0HSL") and jaws ("F0VJ") at M13 position F0 (see chapter 4).

Particle rates are usually normalized to the proton beam current. However, this normalization was different for different momenta. It is difficult to correct the normalization for the different slit and jaw settings: because of the different ways in which they are produced, cloud muons and surface muons will have different "phase spaces" (distributions in space, angle, and momentum) in the M13 beamline, and so will be affected differently by the slits and jaws.

Rates will still be normalized to proton beam current, but caution must be taken when comparing rates from different momenta. It would be simple and useful for *TWIST* to measure the rates carefully, though the *TWIST* results are not greatly dependent on the beam flux.

7.7.2 Rates at Surface Muon Momenta

The asymmetry values have been measured for surface muons (section 7.4.2) and cloud muons (section 7.4.1); they have also been measured for pions, for both U and D scintillators (section 7.4.1). The asymmetry of the beam for a given CP bin (as shown in figure 7.13) can therefore be used to determine how many cloud muons or pions are contaminating the

surface muon beam in that CP bin.

Let α_T be the total asymmetry for a given CP bin, α_s, α_c and α_π be the surface muon, cloud muon, and pion asymmetries, N_T be the total number of counts in the bin, and N_s, N_c, and N_π be the number of surface muons, cloud muons, and pions in the bin. From table 7.1 (and using the average of U and D scintillator data), $\alpha_s = 0.247 \pm 0.001$, $\alpha_c = -0.079 \pm 0.003$, and (for just the D scintillator), $\alpha_\pi = 0.033 \pm 0.006$.

Since the pion and cloud muon distributions do not overlap at this momentum (figure 7.4), $N_s = N_T - N_c$ or $N_s = N_T - N_\pi$, depending on which bin is being considered. Let i represent c or π.

The total asymmetry α_T will be the average of the asymmetries of each particle in the beam:

$$\alpha_T = \frac{\alpha_s N_s + \alpha_i N_i}{N_T}. \tag{7.5}$$

Using $N_s = N_T - N_i$ in eqn. 7.5 and solving for N_s gives

$$N_s = N_T \frac{(\alpha_T - \alpha_i)}{(\alpha_s - \alpha_i)} \tag{7.6}$$

The uncertainty δN_s is found with the standard error formula:

$$\delta N_s = \left[\left(\frac{\partial N_s}{\partial N_T} \delta N_T \right)^2 + \left(\frac{\partial N_s}{\partial \alpha_T} \delta \alpha_T \right)^2 + \left(\frac{\partial N_s}{\partial \alpha_s} \delta \alpha_s \right)^2 + \left(\frac{\partial N_s}{\partial \alpha_i} \delta \alpha_i \right)^2 \right]^{1/2} \tag{7.7}$$

$$= \left[\left(\frac{\alpha_T - \alpha_i}{\alpha_s - \alpha_i} \delta N_T \right)^2 + \left(\frac{N_T}{(\alpha_s - \alpha_i)^2} \delta \alpha_T \right)^2 + \right. \tag{7.8}$$

$$\left. \left(\frac{N_T(\alpha_T - \alpha_i)}{(\alpha_s - \alpha_i)^2} \delta \alpha_s \right)^2 + \left(\frac{N_T(\alpha_s - \alpha_T)}{(\alpha_s - \alpha_i)^2} \delta \alpha_i \right)^2 \right]^{1/2} \tag{7.9}$$

N_c or N_π is then calculated from $N_s = N_T - N_i$.

Once the integrated proton beam current B has been calculated from the T1ION count T using equation 7.4, the normalized particle rate can be calculated as $R = N/B$. This gives the rate in counts per μA·s of proton current.

Table 7.3 lists the results of these calculations, for the D scintillator data at 29.2 MeV/c.

Table 7.4 shows the same calculations for 26.3 MeV/c data. Again, note that the pions, if any, should overlap with the cloud muons, by time-of-flight calculations. The pion rate is very low in this momentum region, however, making it difficult to find direct evidence of them in this plot.

Table 7.5 has a summary of *total* particle rates, relative to total beam rates, for both 26.3 and 29.2 MeV/c.

CP bin (ns)	R_T $(1/\mu A{\cdot}s)\times10^{-3}$	α_T	R_s $(1/\mu A{\cdot}s)\times10^{-3}$	R_c $(1/\mu A{\cdot}s)\times10^{-3}$	R_c/R_s
2	2.00 ± 0.08	0.212 ± 0.007	1.80 ± 0.08	0.18 ± 0.06	0.10 ± 0.03
4	3.8 ± 0.2	0.172 ± 0.005	3.0 ± 0.1	0.84 ± 0.08	0.28 ± 0.02
6	7.0 ± 0.2	0.198 ± 0.004	6.0 ± 0.2	1.0 ± 0.1	0.16 ± 0.02
8	7.6 ± 0.4	0.229 ± 0.003	7.2 ± 0.4	0.3 ± 0.1	0.04 ± 0.01
CP bin (ns)	R_T $(1/\mu A{\cdot}s)\times10^{-3}$	α_T	R_s $(1/\mu A{\cdot}s)\times10^{-3}$	R_π $(1/\mu A{\cdot}s)\times10^{-3}$	R_π/R_s
42	2.18 ± 0.08	0.221 ± 0.006	2.0 ± 0.1	0.20 ± 0.06	0.11 ± 0.03
44	2.4 ± 0.1	0.224 ± 0.006	2.2 ± 0.1	0.20 ± 0.08	0.09 ± 0.03

Table 7.3: Surface muon, cloud muon, and pion rates vs. CP TOF bin, at 29.2 MeV/c; calculated using total beam asymmetry. For this data, **the F0 Horizontal Slit (F0HSL) was set to 60 mm**, and **the F0 Vertical Jaws (F0VJ) were set to 30 mm** (see Chapter 4). CP bins and N_T and α_T values are from figure 7.13. Uncertainties are statistical.

CP bin (ns)	R_T $(1/\mu A{\cdot}s)\times10^{-3}$	α_T	R_s $(1/\mu A{\cdot}s)\times10^{-3}$	R_c $(1/\mu A{\cdot}s)\times10^{-3}$	R_c/R_s
3	9.8 ± 0.4	0.17 ± 0.01	7.6 ± 0.4	2.2 ± 0.4	0.29 ± 0.05
5	20.6 ± 0.8	0.18 ± 0.01	16.6 ± 0.8	4.0 ± 0.8	0.24 ± 0.05
7	25.8 ± 0.8	0.203 ± 0.008	23 ± 1	3.2 ± 0.8	0.14 ± 0.03
9	24.4 ± 0.8	0.226 ± 0.009	23.4 ± 0.8	1.2 ± 0.8	0.05 ± 0.03
11	23.4 ± 0.8	0.238 ± 0.009	24 ± 1	0.2 ± 0.8	0.01 ± 0.03

Table 7.4: Surface muon and cloud muon rates at 26.3 MeV/c; calculated using total beam asymmetry. For this data, **the F0 Horizontal Slit (F0HSL) was set to 69 mm**, and **the F0 Vertical Jaws (F0VJ) were set to 36 mm** (see Chapter 4). CP bins and N_T and α_T values are from figure 7.15. Uncertainties are statistical.

Momentum (MeV/c)	R_s/R_{tot}	R_c/R_{tot}	R_π/R_{tot}
26.3	0.967 ± 0.005	0.033 ± 0.005	0*
29.2	0.971 ± 0.002	0.024 ± 0.002	0.004 ± 0.001

Table 7.5: Particle rates relative to total beam rate, 26.3 and 29.2 MeV/c. (*No pions were detected in the 26.3 MeV/c data.) See tables 7.3 and 7.4 for slit and jaw settings.

Momentum (MeV/c)	R_c (μ_c/μA·s)	R_π (π/μA·s)	R_π/R_c	F0HSL (mm)	F0VJ (mm)
32.1	0.39 ± 0.02	0.168 ± 0.007	0.374 ± 0.004	85	43
35.0	0.45 ± 0.02	0.34 ± 0.01	0.558 ± 0.003	76	35

Table 7.6: Cloud muon and pion rates at 32.1 and 35.0 MeV/c (C scintillator); calculated using direct counts in CP TOF spectrum. Uncertainties are statistical.

Momentum (MeV/c)	R_c/R_{tot}	R_π/R_{tot}
32.1	0.70 ± 0.01	0.30 ± 0.01
35.0	0.57 ± 0.01	0.43 ± 0.01

Table 7.7: Total particle rates relative to total beam rate, 32.1 and 35.0 MeV/c. See table 7.6 for slit and jaw settings.

7.7.3 Rates at Cloud Muon Momenta

Calculating relative rates at cloud muon momenta is simplified by the fact that pions and cloud muons occur separately in the CP TOF distribution (figure 7.6). Table 7.6 lists the sums of the peaks measured for pions and cloud muons, and their ratio, for the two cloud muon momentum data sets (taken at 32.1 and 35.0 MeV/c). The F0 slit and jaw settings are also listed, for comparison; they are similar, but not exactly the same, so care should be taken when comparing rates from these two data sets.

Table 7.7 has a summary of *total* particle rates, relative to total beam rates, for both 32.1 and 35.0 MeV/c.

7.8 Producing a Low-Polarization Muon Beam

As the polarization of cloud muons is opposite to that of surface muons, in theory it is possible to select a channel momentum where the beam polarization is zero (or at least very small). This possibility can be investigated using the momentum scans discussed in section 4.4, as well as polarization and rate results discussed above.

Figure 7.21 shows the total C scintillator[3] count rate as a function of momentum, as measured in the 30 October, 2000, momentum scan. From this figure the pion and cloud muon rates appear to vary linearly with momentum.

For this data, the F0 Horizontal Slit (F0HSL) was set to 80 mm, and the F0 Vertical Jaws (F0VJ) were set to 15 mm. The momentum bite was $dp/p = 2.1\%$.

We can project the ratio N_π/N_c through the range of momenta covered by the momentum scans. This provides an estimate of how much of the "tail" ($p \gtrsim 31$ MeV/c) of the momentum

[3] C is sensitive to muons and pions but almost completely insensitive to positrons; the F scintillator is also used as a positron veto, so these counts should have very few positrons in them.

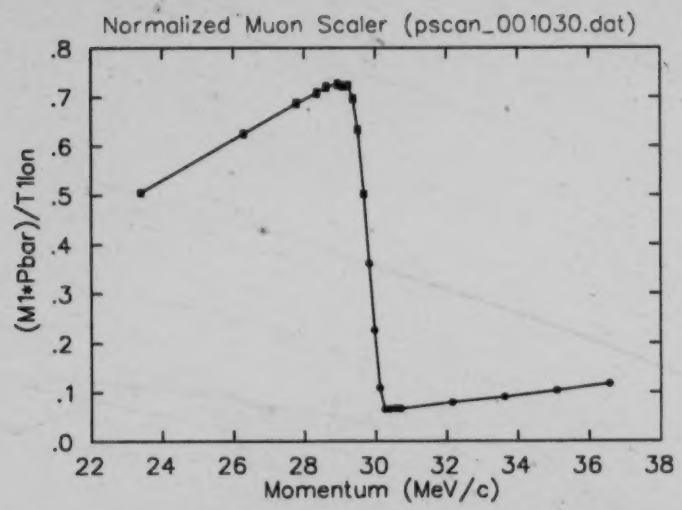

Figure 7.21: C scintillator rate vs. momentum, across surface muon edge. (30 Oct. data) Data is normalized to T1ION scaler. F0HSL = 80 mm, F0VJ = 15 mm, for this data.

scan is pions, and how much is cloud muons. All this information can be projected back below the surface muon distribution.

Although the surface muon rate falls off at the 29.79 MeV/c edge, the CP Time-of-Flight structure of the distribution (which is simply the shape of the pion decay curve) remains unchanged as long as there are surface muons in the beam. If N_{sB} is the number of surface muons in a certain group of CP bins (for example, the CP bins containing cloud muons), and N_{sT} is the total number of surface muons in the distribution, the ratio N_{sB}/N_{sT} should remain constant as momentum changes. Since the CP time of flight of cloud muons and surface muons changes in exactly the same way as momentum varies, the cloud muon peak remains in the same position relative to the surface muon distribution. We can therefore determine what fraction of the surface muons arrive with the same CP TOF as cloud muons, in effect making a "virtual CP cut".

Figures 7.22 and 7.23 show estimates of the surface and cloud muon rates as functions of channel momentum, as well as the resulting beam polarization. These are found by working out the rates of surface and cloud muons for each data point in figure 7.21 using the projection of the "tail" described above, and correcting the surface muon rates by the virtual CP cut. Figure 7.22 uses the entire cloud muon peak region ($\sim$ 9 ns wide CP cut), while figure 7.23 only considers a 2 ns CP bin at the very peak of the cloud muon distribution.

Since the polarization of cloud muons is -0.30 ± 0.02 with respect to surface muons, $N_s = (0.30 \pm 0.02)N_c$ for an unpolarized beam. From table 7.6, the cloud muon rate is

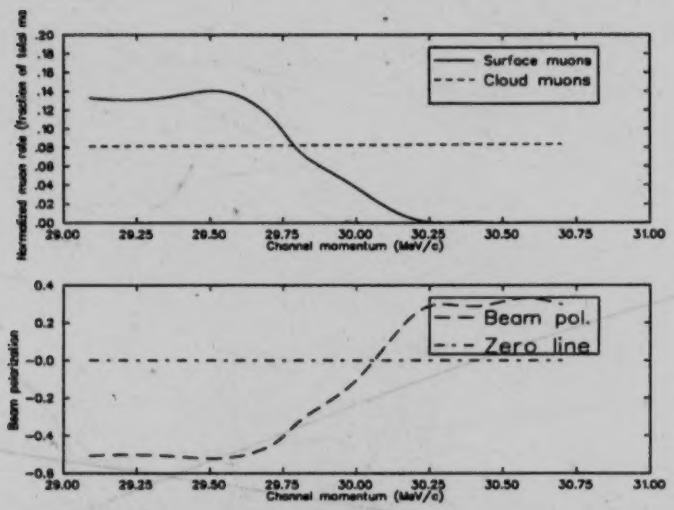

Figure 7.22: Estimated surface and cloud muon rates, and beam polarization, vs. momentum; 9 ns "virtual CP cut" (whole cloud muon distribution).

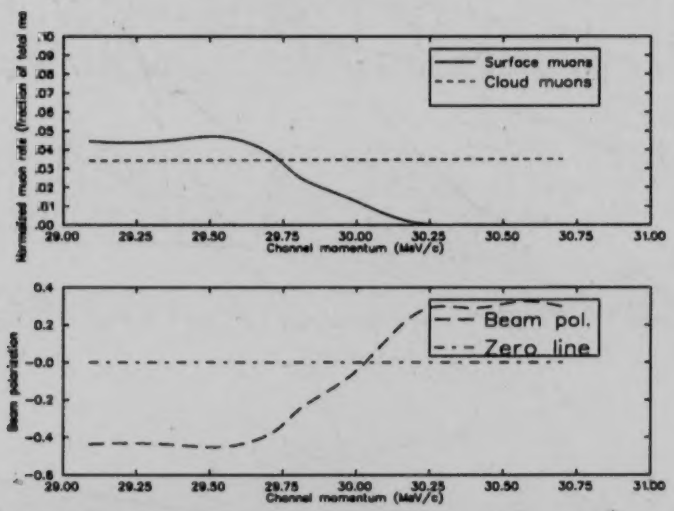

Figure 7.23: Estimated surface and cloud muon rates, and beam polarization, vs. momentum; 2 ns "virtual CP cut" (cloud muon peak only).

CP cut	p_0 (MeV/c)	$P(p_0 - 0.1\%)$	$P(p_0 + 0.1\%)$
9 ns	30.06	-0.06	+0.06
2 ns	30.03	-0.05	+0.05

Table 7.8: Estimates of the momentum where the beam polarization is zero, for two CP cuts. The cuts represent the entire cloud muon region (9 ns cut) and just the cloud muon peak (2 ns cut). p_0 is the momentum where beam polarization $P(p_0) = 0$. The estimated precision to which the channel momentum can be controlled is $\pm 0.1\%$.

about 0.4 μ_c/μA·s (depending on the slit and jaw settings), so the rate of unpolarized beam would be about $(0.4)(1 + 0.30) \approx 0.5$ muons per μA·s of integrated proton beam current.

This technique can be used to estimate at what channel momentum the muon beam is unpolarized (with an appropriate CP cut). However, the exact momentum for unpolarized beam depends on the momentum bite, the slit and jaw settings, and probably the M13 tune. The best way to find this momentum is probably to step the channel momentum and measure the polarization at each step, for the M13 configuration to be used. The technique described above does provide an estimate of the precision to which the beam can be made unpolarized, though. Table 7.8 shows these results for the two CP cuts considered. The channel momentum can be controlled to roughly $\pm 0.1\%$, so as the table shows **the beam polarization can be made zero to within about 5%.**

Chapter 8

Conclusion

"Surface" muons, from pions decaying at rest near the surface of the production target, are highly polarized, and are to be used for the *TWIST* study of the muon decay spectrum. "Cloud" muons, the products of in-flight pion decays, have a much lower polarization. The polarization of these background muons was measured, and the beam's time-of-flight structure was measured to examine the possibility of eliminating cloud muons and pions from the data using a cut on time of flight.

Cloud muons were found to have a polarization of 0.30 ± 0.02, in the direction opposite the surface muon polarization. At a beam momentum of 29.2 MeV/c, the beam composition was found to be: $(97.1 \pm 0.2)\%$ surface muons; $(2.4 \pm 0.2)\%$ cloud muons; and $(0.4 \pm 0.1)\%$ pions. A cut on particle time of flight from the production target to the detector can eliminate pions and cloud muons to better than one part in 10^4, while keeping more than 50% of the surface muons.

A beam of low-polarization muons can be useful, both for calibrating the energy scale of the *TWIST* detector, and for measuring the ρ parameter of the Michel muon decay spectrum. It was found that, by careful selection of the beam momentum to control the relative rates of cloud and surface muons, and using a time-of-flight cut to keep the ratio of cloud to surface muons high, a beam of muons with polarization of about $(0 \pm 5)\%$ can be produced, at a rate of about 0.5 muons per μA·s of integrated proton beam current.

Bibliography

[1] Pierre-André Amaudruz. Midas @ TRIUMF. <http://midas.triumf.ca/>, 2000.

[2] J.H. Brewer. Muon spin rotation/relaxation/resonance. In G.L. Trigg, editor, *Encyclopedia of Applied Physics*, volume 11 (*Mößbauer Effect* to *Nuclear Structure*), pages 22–53. VCH Publishers, Inc., 1994.

[3] Joseph L. Chuma. PHYSICA homepage. <http://www.triumf.ca/people/chuma/physica/homepage.html>, 2000.

[4] Jaap Doornbos. The tuning of M13 for TWIST, theory and some results. Technical Note TN-51, TRIUMF TWIST experiment, 20 December, 2000.

[5] Peter E.W. Green. NOVA data analysis software. <http://daq.triumf.ca/nova/>, 2000.

[6] Application Software Group. Geant—detector description and simulation tool. <http://wwwinfo.cern.ch/asd/geant/>.

[7] Particle Data Group. *Review of Particle Physics*, volume C of *The European Physical Journal*. Springer-Verlag, 1998.

[8] Robert P. MacDonald. Summary of m13 momentum scans of surface muon edge. Technical Note TN-52, TRIUMF TWIST Experiment, 8 March 2001.

[9] L. Michel. Interaction between four half-spin particles and the decay of the μ-meson. *Proceedings of the Physical Society, A*, 63:514, 1371, 1950.

[10] N. Rodning et al. Experiment E614 at TRIUMF: A close look at muon decay. In *Lake Louise Winter Institute*, volume 14, pages 510–519. World Scientific, May 1999.

[11] Martin Shotter. Backgrounds due to pions in beam. Technical Note 35, TRIUMF TWIST experiment, 25 August, 1999.

[12] Farhana Sobratee. M11 channel at triumf, another surface muon source. Master's thesis, University of Alberta, Edmonton, Alberta, Canada, Spring 2000.

[13] C. Tschalär. Muon spectra from pion production targets. Technical Report LA-7222-MS, Los Alamos Scientific Laboratory, University of California, June 1978.

Appendix A

μSR Electronics

This chapter contains schematics of the electronics used in taking μSR data for this experiment, along with brief descriptions. See section 6.2 for more details of the physical apparatus.

The analog scintillator signals were passed through constant-fraction discriminators (which are less prone to signal "walk", or timing errors, due to pulse size fluctuations and noise) to generate logic pulses to be used by the rest of the electronics.

Data was read out using a CAMAC interface.

The following are some of the non-standard abbreviations and symbols used in this appendix:

DAQ	Data Acquisition (read CAMAC modules and record data).
ADC	Analog-to-Digital Converter; measures pulse height.
TDC	Time-to-Digital Converter; measures time between START and STOP pulses.
2228A	TDC used to measure CP Time-of-Flight (see section 7.2.2). Not as precise as the 4208.
4208	TDC used to measure muon decay time. More precise than the 2228A. Channels can be coupled to count pile-up—if channels 3 and 4 are coupled, for example, and a second hit comes into channel 3 while a first hit is waiting to be read out, the second hit is stored in channel 4.
C212	CAMAC input register.
CS	CAMAC Scaler, to be included with the data.
VS	Visual Scaler, for monitoring.
GG	Gate Generator
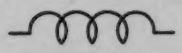	Delay line.
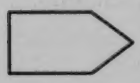	Discriminator.

An arrow indicates a signal sent to either another diagram or the data acquisition system.

An OR gate is used to represent a fan-in/fan-out.

The scintillator arrangement is shown in figure A.1. Coincidences between pairs of scintillators are used as signals for the rest of the electronics. Figure A.2 shows the electronics used to generate the coincidences.

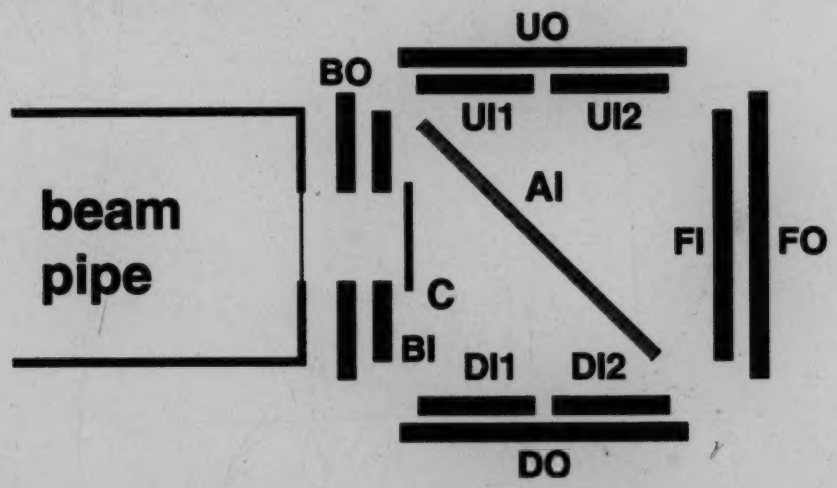

Figure A.1: Scintillator arrangement for μSR beam study. A coincidence within the Inner and Outer scintillators (eg. $FI \cdot FO$) is required for a signal to be used. There is a hole in both Backward (B) scintillators for the incident beam. The Inner U and D scintillators are each split in two; a coincidence is only required with one of them to generate a U or D signal (eg. $UI1 \cdot UO$, not $UI1 \cdot UI2 \cdot UO$); see figure A.2.

Figure A.3 is the schematic for the rest of the data acquisition electronics.

A pile-up gate (PUG) was used to prevent a second muon trigger while the "event gate" (which allows the TDC's to acquire, waiting for the decay positron) is active; the PUG also sets a bit in the C212 input register to signify that a second muon was detected on that event. A pair of coupled channels in the 4208 TDC were used to measure the timing of the pile-up muons.

An inhibit circuit ("INH") was used to prevent new triggers and new data acquisition during certain stages of an event: DAQ startup (opening gates, etc.), Computer Busy (waiting for the computer to read out the CAMAC modules), and DAQ reset (clearing the CAMAC modules for the next event). This signal was coupled with a pulse generator to measure the fraction of time the system was inhibited.

The start of the event gate was used to start a timer in the 2228A TDC. The next pulse from the Capacitive Probe stopped the timer. This measured the CP Time-of-Flight.

The event gate removes the veto on the 821 Discriminator, allowing signals from the positron scintillators through to the 4208 TDC.

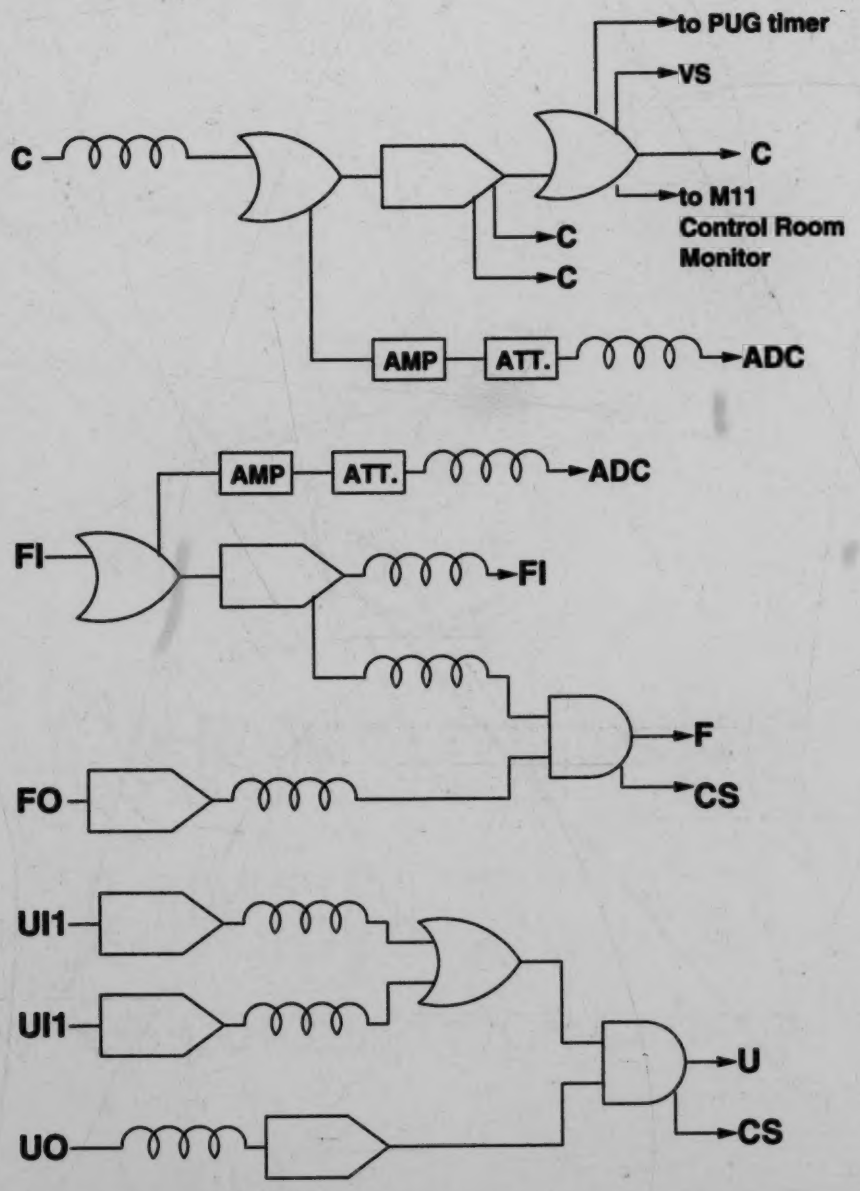

Figure A.2: Electronics for generating scintillator coincidence signals. Circuit for D scintillators is identical to that for U. Circuit for B scintillators is identical to that for F, except that no ADC was used on BI.

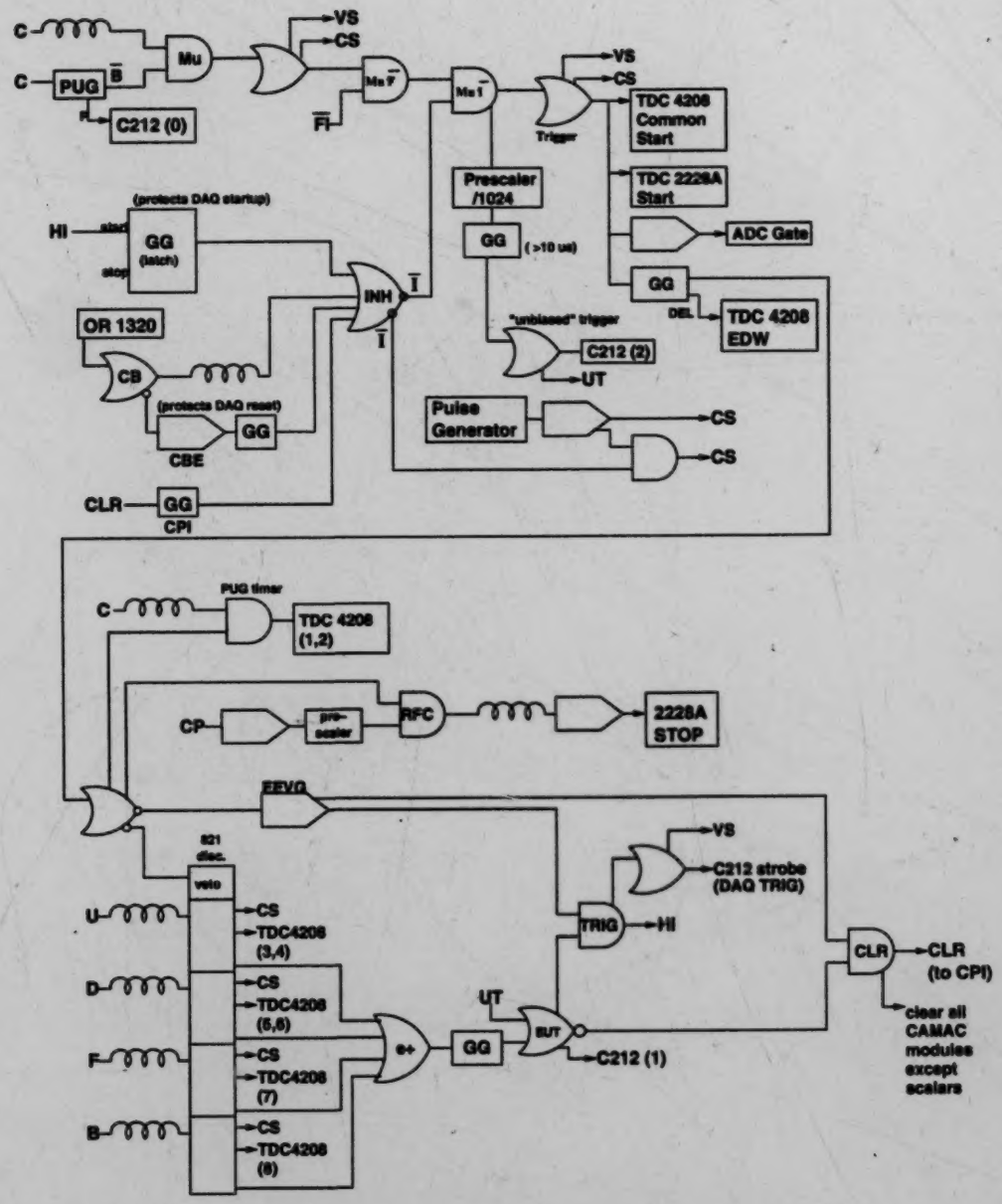

Figure A.3: Schematic for data acquisition electronics.

Index

μSR equation, *22*
μSR spectrometer, **22**, *26*, **27**
μSR equation, 24, 42
1AT1, *30*

ADC cut, 36, 40, 41
apparatus, *26*, **27**
asymmetry, 24, 43

beamline, *11*

capacitive probe, 11, *35*
cloud muons
    definition, 15
CP Time of Flight, 40
CP Time-of-Flight, *35*
CP TOF, *35*, 40
cyclotron period, 11

DAQ, *29*
data acquisition, *29*
decay asymmetry, 43

LAMPF, *26*, **27**

M13, *11*
M13 length, 28
Michel parameters, *4*, *22*
Midas, 35
momentum bite, 16
momentum scan, *15*
muon decay spectrum, *22*, 42

Nova, 35

particle identification, *40*
    beam scintillator ADC, *41*
    CP Time of Flight, *40*
phase space, *13*, 56
Physica, 35
pile-up gate, 29
polarization, *42*, *44*, *46*
    cloud muons, 44
    pions, 45
    summary table, 44
    surface muons, 49
    unpolarized beam, *59*
precession frequency, 24
production target, *30*
proton beam current, 11
PUG, 29

rates, *55*

surface muon edge, 16
surface muons
    definition, 15
    momentum, 14
    polarization, 15
system busy signal, 29

T1 Ion Chamber, 11
T1ION, 11, *55*
TDC calibration, *30*
    random trigger, 33
    time calibrator, 30
Time of Flight, 26, *35*
trigger, 29

unpolarized beam, *59*

weak coupling constants, *3*